

NASA/CR-2002-211425



Design, Fabrication and Testing of a Crushable Energy Absorber for a Passive Earth Entry Vehicle

Sotiris Kellas
Veridian Systems Division
Fairfax, Virginia

April 2002

The NASA STI Program Office . . . in Profile

Since its founding, NASA has been dedicated to the advancement of aeronautics and space science. The NASA Scientific and Technical Information (STI) Program Office plays a key part in helping NASA maintain this important role.

The NASA STI Program Office is operated by Langley Research Center, the lead center for NASA's scientific and technical information. The NASA STI Program Office provides access to the NASA STI Database, the largest collection of aeronautical and space science STI in the world. The Program Office is also NASA's institutional mechanism for disseminating the results of its research and development activities. These results are published by NASA in the NASA STI Report Series, which includes the following report types:

- **TECHNICAL PUBLICATION.** Reports of completed research or a major significant phase of research that present the results of NASA programs and include extensive data or theoretical analysis. Includes compilations of significant scientific and technical data and information deemed to be of continuing reference value. NASA counterpart of peer-reviewed formal professional papers, but having less stringent limitations on manuscript length and extent of graphic presentations.
- **TECHNICAL MEMORANDUM.** Scientific and technical findings that are preliminary or of specialized interest, e.g., quick release reports, working papers, and bibliographies that contain minimal annotation. Does not contain extensive analysis.
- **CONTRACTOR REPORT.** Scientific and technical findings by NASA-sponsored contractors and grantees.
- **CONFERENCE PUBLICATION.** Collected papers from scientific and technical conferences, symposia, seminars, or other meetings sponsored or co-sponsored by NASA.
- **SPECIAL PUBLICATION.** Scientific, technical, or historical information from NASA programs, projects, and missions, often concerned with subjects having substantial public interest.

TECHNICAL TRANSLATION. English-language translations of foreign scientific and technical material pertinent to NASA's mission.

Specialized services that complement the STI Program Office's diverse offerings include creating custom thesauri, building customized databases, organizing and publishing research results . . . even providing videos.

For more information about the NASA STI Program Office, see the following:

- Access the NASA STI Program Home Page at <http://www.sti.nasa.gov>
- Email your question via the Internet to help@sti.nasa.gov
- Fax your question to the NASA STI Help Desk at (301) 621-0134
- Telephone the NASA STI Help Desk at (301) 621-0390
- Write to:
NASA STI Help Desk
NASA Center for AeroSpace Information
7121 Standard Drive
Hanover, MD 21076-1320

NASA/CR-2002-211425



Design, Fabrication and Testing of a Crushable Energy Absorber for a Passive Earth Entry Vehicle

Sotiris Kellas
Veridian Systems Division
Fairfax, Virginia

National Aeronautics and
Space Administration

Langley Research Center
Hampton, Virginia 23681-2199

Prepared for Langley Research Center
under Purchase Order L-13998

April 2002

Available from:

NASA Center for AeroSpace Information (CASI)
7121 Standard Drive
Hanover, MD 21076-1320
(301) 621-0390

National Technical Information Service (NTIS)
5285 Port Royal Road
Springfield, VA 22161-2171
(703) 605-6000

Abstract

A conceptual study was performed to investigate the impact response of a crushable energy absorber for a passive Earth entry vehicle. The spherical energy-absorbing concept consisted of a foam-filled composite cellular structure capable of omni-directional impact-load attenuation as well as penetration resistance. Five composite cellular samples of hemispherical geometry were fabricated and tested dynamically with impact speeds varying from 30 to 42 m/s. Theoretical crush load predictions were obtained with the aid of a generalized theory which accounts for the energy dissipated during the folding deformation of the cell-walls. Excellent correlation was obtained between theoretical predictions and experimental tests on characteristic cell-web intersections. Good correlation of theory with experiment was also found to exist for the more complex spherical cellular structures. All preliminary design requirements were met by the cellular structure concept, which exhibited a near-ideal sustained crush-load and approximately 90% crush stroke.

Introduction

It is widely believed that the inevitable manned exploration of Mars will be preceded by a Mars sample return mission. When samples are collected from the surface of Mars and shipped back to Earth, there exist several options for the final leg of the mission through the Earth's atmosphere and final impact with the Earth's surface. To ensure sample containment, a highly reliable system is required. It can be argued¹ that the reliability of an Earth Entry Vehicle, EEV, can be enhanced if all active systems such as parachute, airbag, or other deployable systems are eliminated. Such an EEV will rely solely on a crushable energy absorber to cushion the payload during a hard surface landing, and such a vehicle is referred to as the passive EEV¹.

In general, the design approach for a passive energy-absorbing system depends on the relative speed of impact and the mass and/or fragility of the payload. For relatively fragile articles or for low-speed impacts where all of the energy is to be dissipated by the energy absorber (no ground penetration), a hard-shell filled with crushable material encapsulating the fragile article is usually preferred. A typical example of this approach is the shipping package for home electronics where a relatively stiff box acts as a protective shell for the article and energy absorber inside. In the event of an accidental drop, most of the energy is absorbed by deformation of the energy-absorbing material adjacent to the cushioned article, while the box remains relatively intact.

To the contrary, for high-speed/high-mass impacts it is often advantageous to allow some of the impact energy to be dissipated through the plastic deformation of the impact surface. In the case of a relatively sharp object impacting a soft surface, it is even possible to accomplish the entire impact-energy management process through penetration alone. However, for a relatively blunt impacting object a combination of an engineered energy absorber and some impact-surface penetration is needed. For such an event the payload is encapsulated in a relatively rigid shell surrounded by energy-absorbing structure which, at impact, is allowed to crush from the outside first. An example of this approach for high-mass impact includes the modern automobile and in particular the racecar. The driver (payload) is strapped in a relatively rigid cockpit, which is surrounded by frangible structure, the energy absorber. The driver can usually survive most in-plane impacts, especially ones involving deformable crash barriers, as long as the cockpit integrity is not compromised.

The design requirements for an energy absorber are of course dependent on the specific mission goals and the fragility of the payload such that a maximum dynamic load and time duration are not exceeded. Once the energy-absorber crushing strength has been defined by the maximum load requirement, the expected impact velocity and the shape of the crush response are used to establish the crush-stroke, with uniform load versus displacement response resulting in minimum stroke requirement. Payload containment assurance may also be a design requirement due to, for example, sample contamination

issues. Under these circumstances it is necessary to consider the containment assurance of the sample container as well as the integrity of the payload. Other important design parameters related to the condition of the samples include payload environmental exposure, and/or heat transferred from the heat shield of the EEV. When quick retrieval or water impact is not possible, the huge amount of heat energy carried by the vehicle can present a problem unless the heat-shield is ejected prior to impact or is engineered to separate clear of the vehicle during impact. If timely shedding of the heat shield is not possible, the energy absorber may be required also to function as a heat insulator.

Design and verification of the energy-absorbing concept was carried out for a potential mission with the following preliminary design requirements:

- (a) Impact velocity, 39-42 m/s.
- (b) Total effective vehicle mass at impact, 14 kg. This is not the total vehicle mass but rather the mass exerted on the energy absorber at the moment of impact.
- (c) Omni-directional impact capability within a conical angle of $\pm 30^\circ$.
- (d) Maximum dynamic load delivery to the sample container for nominal surface (clay) impact should be less than 2500 G.
- (e) Maximum dynamic load delivery to the sample container during a hard/flat surface impact should be less than 3500 G.
- (f) Provisional requirement: — penetration resistance/containment assurance for various impact surfaces including hard protrusions (rocks) up to 50 mm tall.

Note that the actual dynamic loads imparted on the sample container during impact depend on the container mass and the degree of coupling to the rest of the vehicle. Therefore, the 2500 and 3500 G levels refer to the dynamic loads of the energy absorber that would occur if the container were rigidly attached to the EEV. An additional simplification, related to the lack of appropriate data, involves the vehicle heat shield and supporting structure. For preliminary energy-absorber design and concept verification, it was assumed that all impact energy would be dissipated either by ground penetration (soft surface impact) or a combination of ground penetration and energy absorber crushing (hard surface impact). In other words, heat shield fracturing and crushing does not contribute to the impact-energy management process.

Due to the combination of high impact speed and relatively large impact mass, a “race car”-like concept was thought to be the most appropriate. The chosen energy absorber evolved from a foam-filled cellular type construction previously designed^{2,3} and patented⁴ for use in energy absorbing subfloor aircraft keel-beams. The cellular nature of the design ensured weight efficiency, while the composite cell wall construction offered the option of customizable crush response to meet potential changes in evolving mission requirements. The relatively rapid fabrication capability of prototype structures was also a key

factor in the selection of the concept. The energy absorbing structure was spherical in shape to meet the omni-directional impact design requirements. It consists of a relatively rigid spherical cavity (sample container holder), a surrounding crushable cellular structure, and an outer spherical cover with provision for penetration resistance and load distribution capability. Basic features of the energy absorber are shown in Figure 1.

The crush response of cellular structures is generally dependent on the cell size and shape, the cell wall mechanical properties, the cell wall thickness, and the number of cell walls (flanges or webs) intersected at a junction. In general, the crush strength increases with the number of webs at a junction, due to the improved stability. Progressive crush response of thin-wall metal box sections and intersections have been studied by a number of researchers with the most notable work carried out by Wierzbicki, Abramowicz, Jones and Hayduk, and documented in numerous publications such as references 5–9. Their work involved the mathematical description of the process of energy dissipation at web intersections resulting from empirical observations of the folding mechanisms and their influence on the mean sustained crushing load. According to those researchers, localized deformation and cell wall folding can be classified in two categories, extensional and isometric (inextensional). In the isometric mode, the deformation is often confined to narrow zones, called fold lines. Because the total deformation area is small relative to the entire structure, the isometric mode of energy dissipation is not as efficient as the extensional mode. In practice, the prevailing mode depends on the number of flanges per intersection, and the relative thickness to width of the flanges. Typically, the more stable an intersection is, the more likely the extensional mode will prevail.

While it is recognized that deformation and failure processes in laminated composite materials differ greatly from those in isotropic metals, it has been shown³ that for thin composite cell walls where plastic-like folding is possible, the metallic approach can be employed provided that appropriate material properties can be established. Examples of composite laminates which exhibit plastic-like response include angle-ply laminates or quasi-isotropic laminates with high strain to failure fibers and matrices. Since efficiency is usually of prime interest, hybridization is often used^{2,3} to achieve the quasi-plastic deformation response without a great loss in crush efficiency. Typical hybridization includes glass and kevlar or graphite and kevlar, with glass and/or graphite used for strength and kevlar for post-impact integrity and/or penetration resistance. When elevated temperature is not an issue, polyethylene fiber such as “spectra” could also be used instead of kevlar.

Proof-of-concept was accomplished with the design, fabrication, and dynamic testing of five composite cellular spheres. Sizing of the spheres was carried out through the theoretical crush-load predictions using a modification of the original theory for plastic crush response of metals⁵⁻⁹, coupled with component-level crush testing.

Composite Cellular Sphere Concept

While composite structures are much harder to analyze than metal structures, composites offer unique advantages in fabrication and customizable structural response. The ability to tailor a given structure to meet the changing needs of a mission is particularly important and in many cases it is necessary. Some notable customizable features offered by the composite cellular sphere concept include adjustable sustained crush load, trade-off between crush efficiency and penetration resistance, and wide choice of fabrication techniques and material combinations to meet extreme thermal gradient and/or thermal insulation requirements.

The energy-absorbing concept (and payload) is shown schematically in Figure 1 and consists of three primary components: a relatively rigid inner shell, a crushable foam-filled cellular structure with polar orthotropy (cell axis oriented radially), and an outer shell. The lid of the energy absorber, which is also of cellular construction, is not shown in Figure 1.

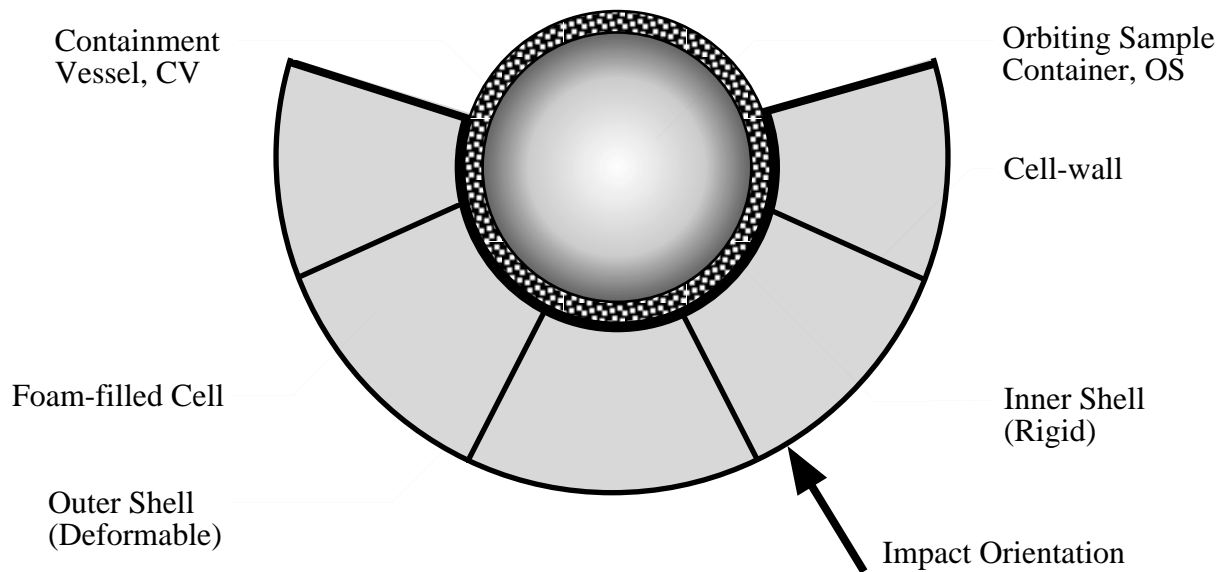


Fig. 1 - Schematic of the cellular sphere impact-energy management concept and sample container.

The crushing load is controlled primarily by the thickness and reinforcement composition of the cell walls, and penetration resistance and load redistribution is controlled by the hybridization of the outer shell. The role of the inner shell is to provide adequate crush load reaction while isolating the sample container from the stress concentrations imparted by the relatively stiff cell walls. The foam core offers thermal insulation, structural stability to the cells, and increased crush energy dissipation. Most importantly it also serves as a mandrel during fabrication. Depending on the relative size between a penetrator and the cell, a substantial degree of penetration resistance can be achieved through penetrator

wedging and/or cell wall crushing. In this case, cell wall reinforcement with tough fibers such as kevlar is essential.

Cellular Sphere Geometry

Before a cellular sphere can be constructed, a choice of cell geometry and cell density is required. Three practical options for sectioning a spherical surface (or volume) are shown in Figure 2. The preferred choice of cell size and shape depends on the magnitude of the required crush loads and the degree of complexity of the fabrication technique. Typically, the larger the cells the less effective the cellular structure is in dissipating energy. Also, for a given crush load, the larger cells contain stronger cell walls which produce a more severe stress concentration at the inner shell interface. However, the more cells the spherical surface is divided into, the more intricate and tedious the fabrication process becomes. Moreover, the complexity of fabrication depends on whether a single cell shape is used to assemble the sphere or a combination of more than one.

For the practical purpose of producing a cellular structure, a spherical surface can be divided into twelve regular (spherical) pentagons, such as ABCDE, or sixty isosceles (spherical) triangles, such as OAB, as shown in Figure 2. Since 60 triangles would complicate the fabrication process and 12 pentagons would be too few to allow engagement of an adequate number of web intersections and/or cell walls during impact, a compromise was reached to use the spherical version of the truncated icosahedron, more commonly known as the “soccer ball”. While this approach requires the sphere to be constructed out of two distinct geometric shapes, pentagons and hexagons, instead of just one, it offers a good trade-off between the total number of cells (32) and the number of cell junctions (60). With the soccer ball approach, sufficient homogeneity is achieved due to the relatively high number of cell wall intersections for the total number of cells as compared to, for example, 32 intersections per 60 cells for the triangular cell approach. A good balance of homogeneous behavior and crush efficiency is essential for achieving a combination of desirable features such as mass efficiency, omni-directional impact protection, and a manageable stress concentration at the inner shell interface.

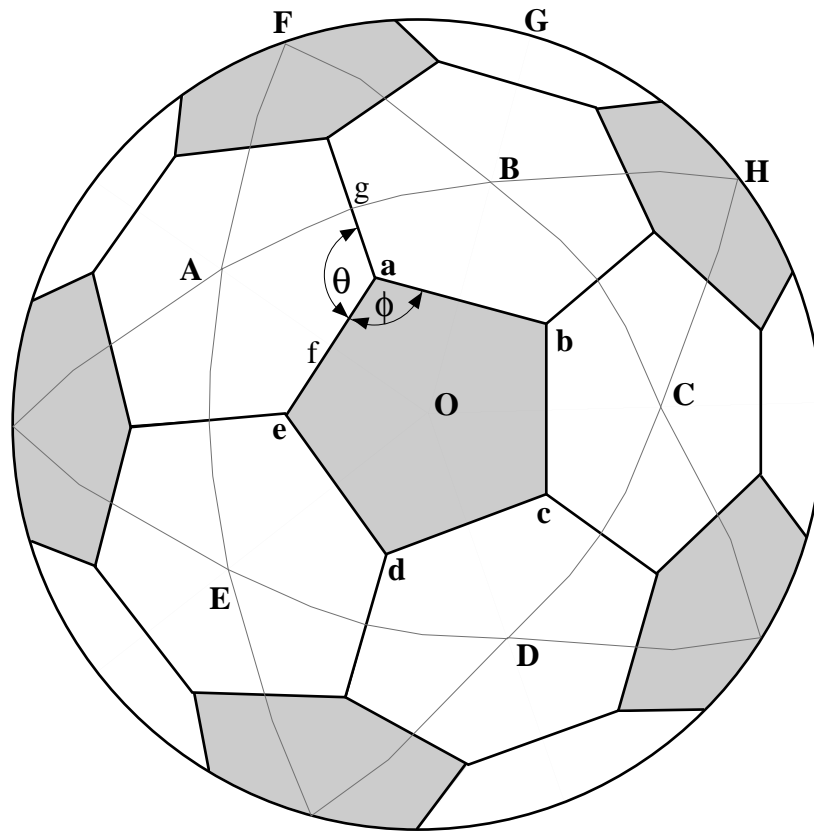


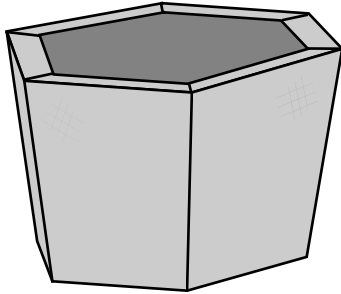
Fig. 2 - For fabrication purposes there are three practical options for segmenting a spherical surface. (a) Twelve spherical pentagons, such as ABCDE, (consisting of 20 junctions and 30 cell-webs), (b) “soccer ball”, combination of twelve pentagons and twenty hexagons (composed of 60 junctions and 90 webs), and (c) sixty isosceles triangles such as OAB (resulting in 32 junctions and 90 webs).

Cellular Sphere Fabrication

Five cellular specimens were fabricated and dynamically tested during the course of this study. All samples were made using the “soccer ball” approach and were hemispherical in shape. The three basic fabrication steps used to construct the cellular spheres are shown schematically in Figure 3. In the first step, pre-shaped foam blocks were wrapped with dry reinforcement fabrics. Graphite layers were typically wrapped first followed by kevlar containment plies. All graphite plies were the same height as the cell, whereas the kevlar had a 13 mm overhang on either end which was folded over and secured to the foam blocks as shown in Figure 3(a). The primary purpose of the kevlar fold-over was to enhance the coupling between the cell walls and the inner/outer shells. A secondary role was to encapsulate the graphite layers and reduce radial thermal conductivity through the graphite plies of the cell walls.

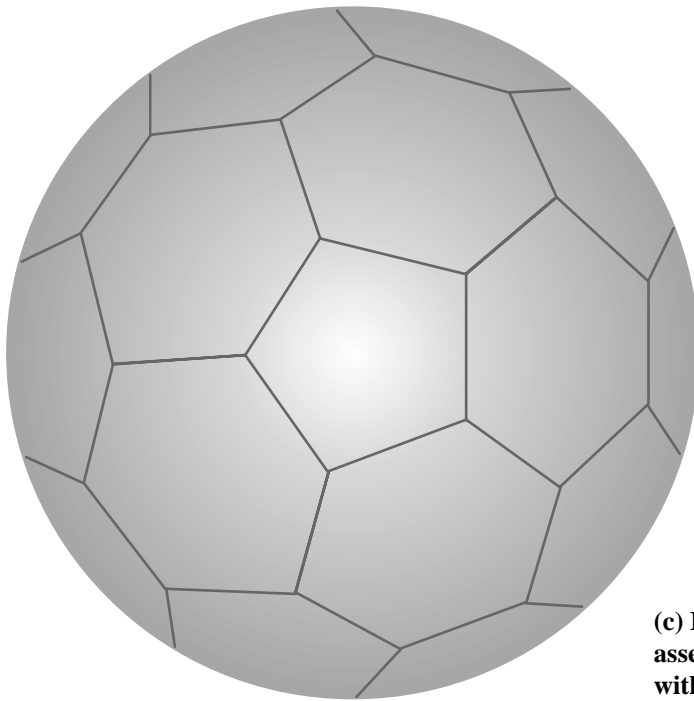
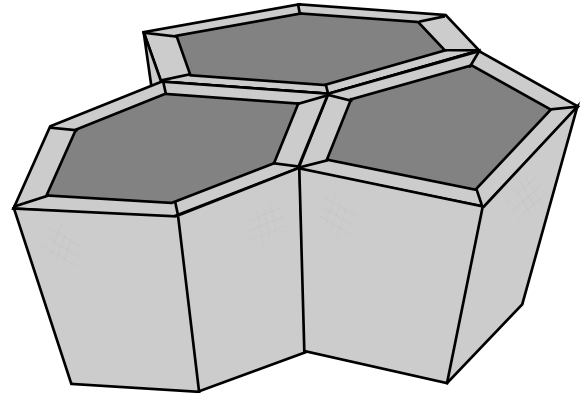
The second step is shown in Figure 3(b) and consisted of the assembly of the fiber-wrapped blocks to form the spherical structure. The outer and inner shells in the form of conformable dry fabric layers were applied in the third step and temporarily secured in place with spray tack adhesive. To complete fabrication, the fully assembled structure was vacuum-sealed, infused with resin and cured according to

the resin manufacturer's suggested cycle. Since the foam cores provided the structure's shape, no additional tooling was necessary, thus allowing potential flexibility in geometric alterations without additional tooling cost.



(a) Closed-cell foam blocks are wrapped with fiber reinforcement. Outer kevlar layer(s) is folded over with 13mm overlap.

(b) Fiber wrapped cells are assembled to form a spherical surface. Tack adhesive is used to hold the blocks together.



(c) Inner and outer shell plies are placed over the assembled cell blocks and the structure is infused with resin and cured.

Fig. 3 - Three basic fabrication steps used in the construction of the cellular-sphere samples. A total of five samples were fabricated using this technique. All samples were hemispherical in shape.

Material Selection

All cellular specimens utilized the same combination of fiber reinforcements and matrix material with some minor variation in stacking sequence and degree of hybridization. For this preliminary study, material selection was based primarily on off-the-shelf material availability and cost. Details of the core materials and composite matrix are summarized in Table 1, and details of the fiber fabrics are listed in Table 2.

Table 1: Foam core Material and Resin Details

Material & Designation	Raw Material Density kg/m ³	Processed Material Density [†] kg/m ³	Cell/Pore Characteristics & Density ppi*	Fabrication Method	Surface Sealing Method	Manufacturer/ Supplier
Polyurethane Foam, PF 1	32	88.40	Rigid/Closed Cell N/A	Expanded	N/A	Fiber Glast Developments, Inc.
Polyurethane Foam, PF 2	32	114.92	Rigid/Closed Cell N/A	Expanded	N/A	Fiber Glast Developments, Inc.
Carbon Foam, CF 1	56	70.09	Rigid/Open Cell 100ppi	Machined to Shape	Lightweight Acrylic filler & Epoxy	ERG Materials & Aerospace Corp.
Carbon Foam, CF 2	73	91.26	Rigid/Open Cell 100ppi	Machined to Shape	Lightweight Acrylic filler & Epoxy	Destech Corporation
Pro-set Epoxy 1171v/237	918	N/A	N/A	Vacuum Infusion	N/A	Gougeon Brothers, Inc.

* A measure of linear porosity — pores per inch.

† Due to the expansion process or applied coating, foam cores were much denser on the surface.

For the first three specimens polyurethane foam cores were expanded in a mold instead of being machined individually. This method was chosen not only for its cost effectiveness but also for the capability of expanding foam cells of custom density. A two-part polyurethane foam was used with the density of the expanded foam being regulated by adjusting the amount of liquid polymer poured into the mold. Carbon foam was identified in earlier studies¹⁰ as the most suitable core material based on its excellent crush energy-absorbing characteristic and, most importantly, for its relatively high-temperature capability. Therefore, machined-to-shape carbon foam cells were used for the last two specimens. The porous carbon-foam cell-cores had to be sealed before being used in conjunction with the resin infusion process. From several available techniques for filling up the surface pores, a simple and relatively inexpensive method was chosen for this study, involving a lightweight acrylic-based paste and a thin overcoat of epoxy resin.

Table 2: Fiber Reinforcement and Fabric Details

Material Designation	Fiber Type	Fiber Count Denier	Tow Density Per cm (inch)	Fabric Architecture	Areal Weight g/m ²	Fabric Thickness mm	Manufacturer or Supplier
Gp	Graphite T-300	3000	4.7/4.7 (12/12)	Plain	193.0	0.25	Northern Fiber Glass Sales Inc.
Gs	Graphite G30-500	3000	9.4/9.4 (24/24)	8H Satin	376.7	0.46	Textile Technologies Inc.
Kp	Aramid Kevlar-129	840	(10.2/10.2) (26/26)	Plain	207.0	0.25	Hexcel Schwebel
Ks	Aramid Kevlar-29	3000	6.7/6.7 (17/17)	8H Satin	474.6	0.58	Fabric Development Inc.

Since no elevated-temperature tests were planned for this preliminary series of testing and evaluation of the cellular sphere concept, a low-temperature cure infusion resin was chosen. A two-part epoxy resin with a very low viscosity and long working time was selected to allow for vacuum-assisted infusion to take place at room temperature.

Fiber reinforcements were chosen for their specific mechanical attributes; whereas, the woven fabrics were simply chosen based on availability at the time of fabrication. No particular effort was made to optimize the structural response by taking advantage of fiber-reinforcement placement with respect to the cell axis. The graphite fibers T-300 and G30 were chosen for their compressive strength and stiffness. The relatively large diameters of these fibers offer better compressive properties than their high tensile strength counterparts. The meta-aramid fibers, kevlar 29 and 129, were chosen for their toughness and high strain to failure. Details on the woven fabric architecture used in the fabrication of the five cellular spheres are summarized in Table 2.

Cell Wall Stacking Sequence

Hybridization of the cell walls was a key factor in achieving a quasi-plastic crush response and a desirable degree of penetration resistance and/or post-crush integrity. It is believed that optimum crush response in a cellular sphere can be achieved only when the entire graphite reinforcement is oriented along the radial and hoop cell direction and the kevlar fiber is arranged at $\pm 45^\circ$ to the hoop direction. Due to the intricate geometric nature of the cells, this could be achieved only with the use of custom-made polar fabrics or some automated computer-controlled fiber-placement technique. For this preliminary study, optimum fiber reinforcement orientation was traded against fabrication convenience and cost with the choice of off-the-shelf biaxial fabrics. Details on the number of plies per cell and stacking sequence are summarized in Table 3 for all five cellular spheres.

Table 3: Composite Cellular Sphere Fabrication Parameters

Spec. No.	Cell Wall [†] Ply Sequence	Cell Wall Thickness Mm	Inner Shell Ply Sequence	Outer Shell Ply Sequence	Foam Core Material	Matrix Material
1	$(Gp_5/Kp^*)_s$	3.40	Gp_3	Kp_2	PF 1	Pro-Set
2	$(Gp_3/Kp^*)_s$	2.08	Gp_3	Kp_2	PF 1	Pro-Set
3	$(Gp_5/Kp^*)_s$	3.23	Gp_3	Kp_2	PF 2	Pro-Set
4a	$(Gp_7/Kp^*)_s$	4.75	Gp_5^{**}	$Gp//Ks_3^{\dagger\dagger}$	CF 1	Pro-Set
4b	$(Gp_7/Kp^*)_s$	4.75	Gp_2^{\ddagger}	$Gp/Kp_2 Gs_2$	CF 2	Pro-Set

* Approximately 13 mm of each kevlar ply was folded over the top and bottom of each foam cell, see Figure 3.

[†] The entire cell wall thickness as formed by two adjacent cells. Cell interface is the plane of symmetry denoted by “s.”

** Additional three layers of the same material were added in a secondary process to repair machining damage.

^{††} The kevlar layers were loosely placed over the cured sphere and were rigidly attached only at the equator using a 19 mm thick band of epoxy resin.

[‡] Three layers of graphite satin fabric were added in a secondary process to built-up the thickness to desirable value.

Due to the conical nature of the foam cores and the bi-directional nature of the fabrics, the fiber orientation was varied continuously as annular fabric cutouts were wrapped around the foam core. For three or more plies, of the same material, a relatively uniform quasi-isotropic laminate was created since at least six such plies were combined to make up each cell wall. To the contrary, for only one ply per cell, as in the case of the kevlar layers in samples 1-3 (see Table 3), quasi-isotropy could not be guaranteed for every cell wall. Nevertheless for the purpose of crush load predictions, the assumption of

quasi-isotropy is used throughout this report and thought to be acceptable, since crush strength is controlled primarily by the graphite reinforcement as long as cell wall tearing is not the predominant mode of energy dissipation. Note that ($\pm 45^\circ$) fabric layers are much more efficient in dissipating energy through tearing compared to an equal number of ($0^\circ/90^\circ$) fabric layers, since there are twice as many fibers engaged in the energy dissipating process in a ($\pm 45^\circ$) layer as opposed to a ($0^\circ/90^\circ$) fabric layer.

Experimental Procedures and Results

Composite cellular sphere samples were sized using a theoretical technique coupled with a series of component-level tests to predict their crush load. Such tests included static tests to determine the effective cell wall yield stress, crush and penetration tests on foam core samples, and static crush tests on plates and “Y” element samples for verification of collapse mode and energy dissipation.

Cell Wall Tests

Three quasi-isotropic laminated panels were fabricated with 8, 12, and 18 plies, corresponding to the three different layups used in the cellular sphere construction. Details from this series of tensile tests are shown in Table 4, and a typical stress/strain response from panel 1 is shown in Figure 4. Tensile coupon specimens were cut from each panel at three orientations (0° , 45° and 90°) with respect to a reference panel-edge. Specimens were typically 25 mm wide and approximately 30 cm long. The highest available test-machine cross-head speed was used (50.8 cm/min.) for all tests. Average ultimate strength data for each panel were used to determine an effective yield stress value, which was subsequently used in the analytical part of this work. While the average value from all three orientations was used in the calculation of the effective yield strength, values corresponding to $0^\circ/90^\circ$ and 45° load orientations are presented separately in Table 4 to highlight the lack of complete in-plane isotropy. Unexpectedly, the largest degree of anisotropy was obtained for panel number 3 as compared to panels 1 and 2. This anomaly was thought to be associated partly with the test method and in particular to the large specimen thickness-to-width ratio which caused a more severe stress concentration at the grip region. Another likely cause is fiber misalignment in favor of the 0° orientation. Despite this anomaly, the trend of the average ultimate strength appears to correlate well with the relative amount of graphite to kevlar reinforcement in each panel, with greater strength achieved in panel 2 (5:1 graphite to kevlar ratio) and lower in panel 1 (3:1 graphite to kevlar ratio).

As shown in Figure 4, the tensile stress/strain response (typical of all three panels) was nearly linear up to the ultimate strength point, which was reached when the graphite plies fractured and delaminated from the kevlar layers. No kevlar-layer failures were observed. Minor deviation from linearity was thought to be associated with slipping and re-gripping of the specimen by the wedge-type jaws. Consequently, the strain indicated in Figure 4 is not a pure material property.

Table 4: Flat Panel — Tensile Test Results

Spec. No.	Flat Panel Stacking Sequence	Cell wall Simulation for Sphere No.	Average Panel Thickness mm	Average Ultimate Strength for 0° & 90° / 45° / All† MPa
1	$(0_{Gp}^{\circ} / 30_{Gp}^{\circ} / 60_{Gp}^{\circ} / 45_{Kp}^{\circ})_S$	2	1.867	335.7* / 363.3† / 344.9
2	$(0_{Gp}^{\circ} / 18_{Gp}^{\circ} / 36_{Gp}^{\circ} / 54_{Gp}^{\circ} / 72_{Gp}^{\circ} / 45_{Kp}^{\circ})_S$	1 & 3	2.718	364.1* / 365.7† / 364.6
3	$(0_{Gp}^{\circ} / 13_{Gp}^{\circ} / 26_{Gp}^{\circ} / 39_{Gp}^{\circ} / 51_{Gp}^{\circ} / 64_{Gp}^{\circ} / 77_{Gp}^{\circ} / 0_{Kp}^{\circ} / 45_{Kp}^{\circ})_S$	4a & 4b	4.089	359.3* / 326.9** / 351.2

* Average of six tests. Three samples were cut parallel (0°) and three were cut normal (90°) to the panel reference edge.

† Average of three tests. Samples were cut at 45° with respect to the panel reference edge.

** One of three specimens tested failed too close to the grip region and its contribution was neglected from the average.

‡ These values were used in the analysis.

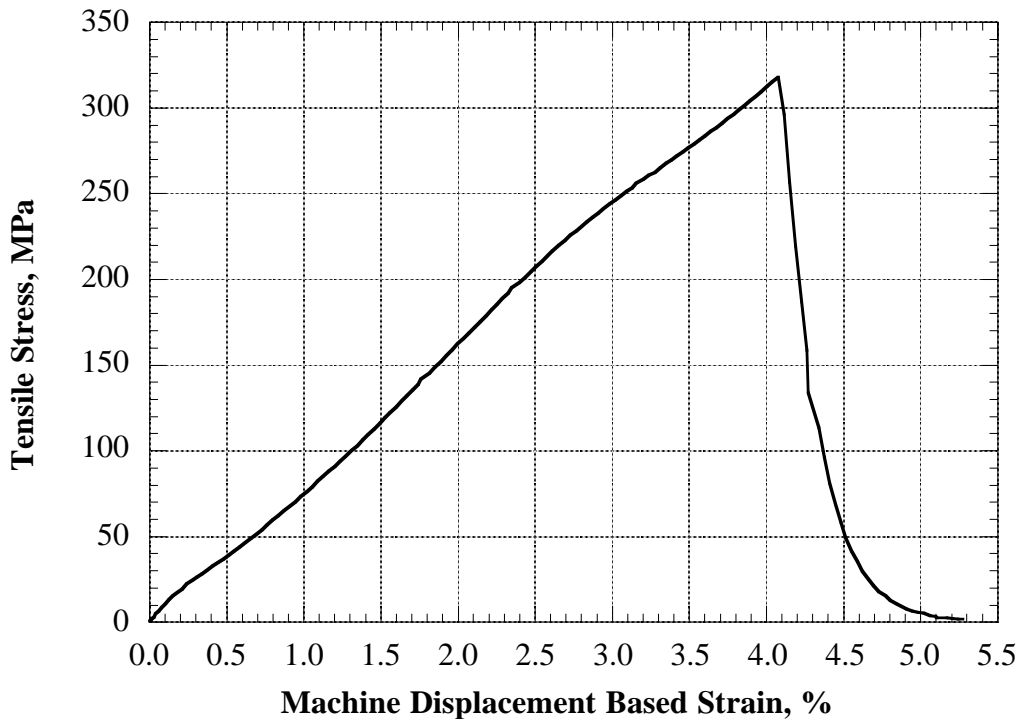


Fig. 4 - Typical tensile stress/strain response of 8-layer coupon specimen with stacking sequence corresponding to sphere 2. Note that with the exception of the ultimate stress point, this represents a typical response for all three types of laminates tested. The test speed was 50.8 cm/min. and the “strain” was determined from the machine cross-head displacement output.

Crush tests were also carried out on flat plates with the aid of a test fixture¹¹ designed to promote localized material crushing rather buckling. These tests were performed to measure the maximum possible crush strength of the webs, which could be achieved if the web edges were simply supported by vertical knife-edges. In principle, the cellular sphere could attain such crush strengths if its cell walls had a large enough thickness to width ratio. A typical example of a pure crush response, representative of the cell walls of sphere 2, is shown in Figure 5 together with a schematic of the test set-up. For these

tests, the crush initiation stress was regulated by the geometry of the machined stipple initiator. The average sustained crush stress for this series of specimens was approximately 76 MPa.

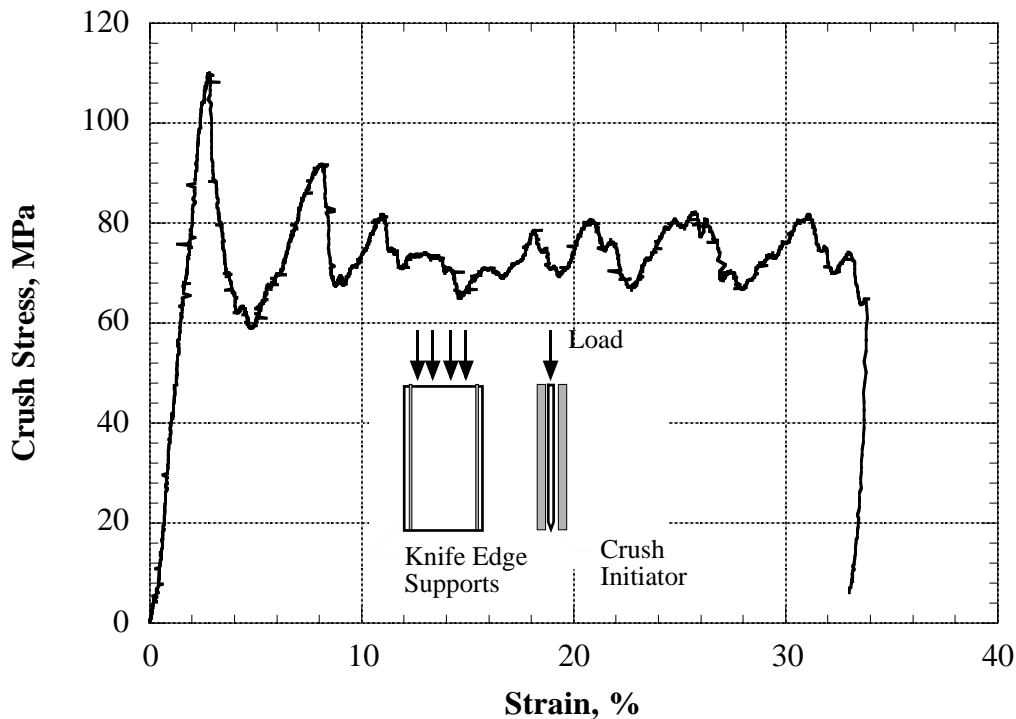


Fig. 5 - Typical edgewise crush test of simply supported flat laminate corresponding to the cell walls of sphere 2. The stacking sequence was $(0^{\circ}_{Gp}/30^{\circ}_{Gp}/60^{\circ}_{Gp}/45^{\circ}_{Kp})_S$, specimen width = 50.8 mm, knife edge spacing = 44.5 mm, specimen height = 76.2 mm. The loading speed was 25.4 mm/min.

Foam-Core Tests

Several candidate core materials were evaluated during the early phase of this program¹⁰ and two were actually chosen and used in the fabrication of cellular sphere samples. These included expanded polyurethane foam of two densities used in spheres 1-3 and carbon foam used in spheres 4a and 4b. Quasi-static penetration tests for the expanded polyurethane samples are summarized in Figure 6. A flat-face cylindrical indenter of 25.4 mm diameter was used in conjunction with cells identical in density and volume to the ones used in the fabrication of cellular spheres. A photograph of indented polyurethane cells together with the indenter is shown in Figure 7. Indentation, instead of crush testing was performed since it is thought to reflect more accurately the mode of energy dissipation of the constrained foam core within the cells and the lateral resistance it imposes during cell wall bending.

Due to the constrained expansion process, polyurethane foam core samples contained a boundary layer of denser material. The effect of the boundary layer on crush strength is highlighted in Figure 6 by the initial peak load (occurring at approximately 10% deformation) followed by a sudden drop associated with the failure of the tougher outer layer of material. As expected, the 30% denser foam (used in

cellular sphere 3) is stronger and also exhibits a higher rate of compaction, as shown in Figure 6. Since no evidence of any substantial rate effect was apparent it was deemed unnecessary to carry out dynamic tests for this core material. Therefore, all effective sustained crush values used in the analysis are derived from the quasi-static tests. Referring to Figure 6, it was assumed that the effective sustained crush strength for the core of cellular spheres 1 and 2 is 1.1 MPa and 1.65 MPa for the core of sphere 3.

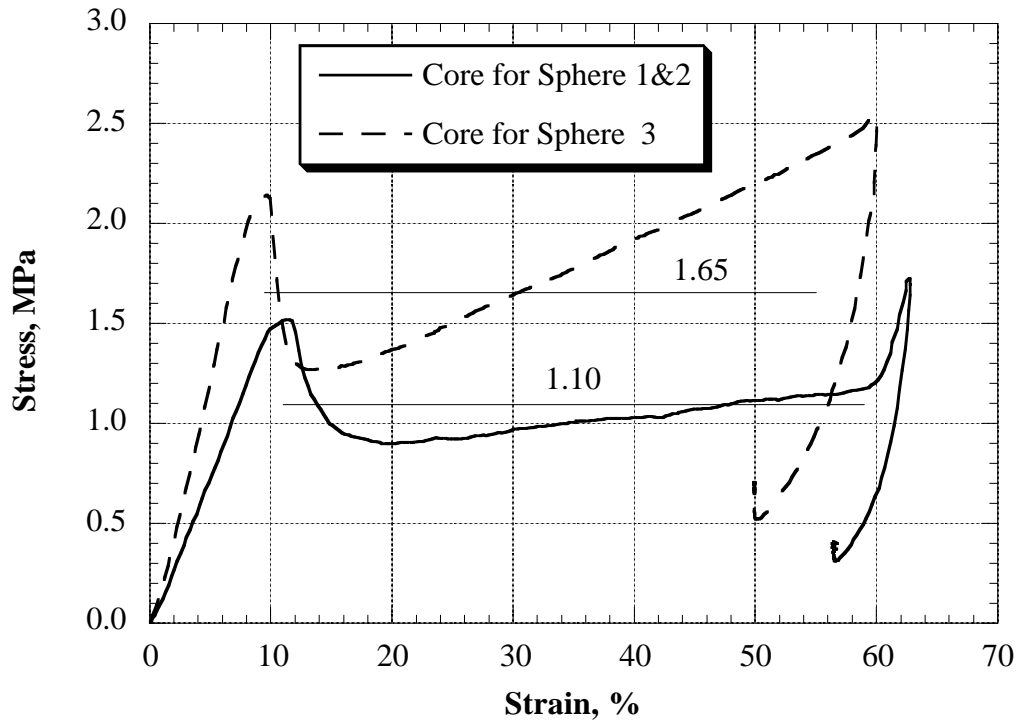


Fig. 6 - Quasi-static penetration tests for expanded polyurethane core samples used in cellular spheres 1-3. Tests were conducted using a flat face (25.4-mm-diam.), cylindrical indenter on actual pentagonal cells identical in density and volume to the ones used for cellular sphere fabrication.

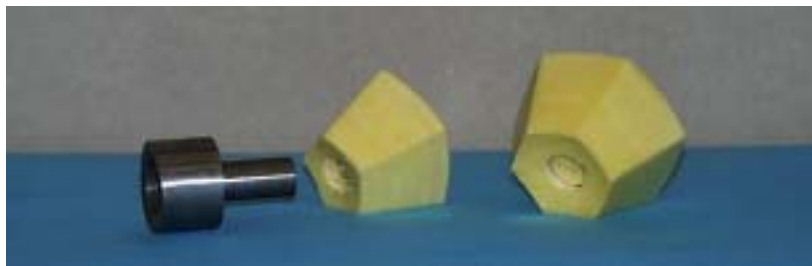


Fig. 7 - Expanded polyurethane cells similar to the ones used in the construction of spheres 1, 2 and 3 which were subjected to partial penetration using a 25.4-mm-diameter flat face indenter.

During preliminary work on candidate core materials¹⁰, carbon foam was identified as a leading material due to its high temperature capability and excellent crush response. In the absence of adequate surrogate material, carbon foam was used in the fabrication of cellular spheres 4a and 4b despite its relatively high

cost compared to polymeric rigid-cell foams. Carbon-foam blocks with sealed surfaces (lightweight acrylic-based paste and a thin overcoat of epoxy resin) were tested statically and dynamically using the same penetration test described earlier. Typical static and dynamic test results for the carbon foam core used in sphere 4a are shown in Figure 8.

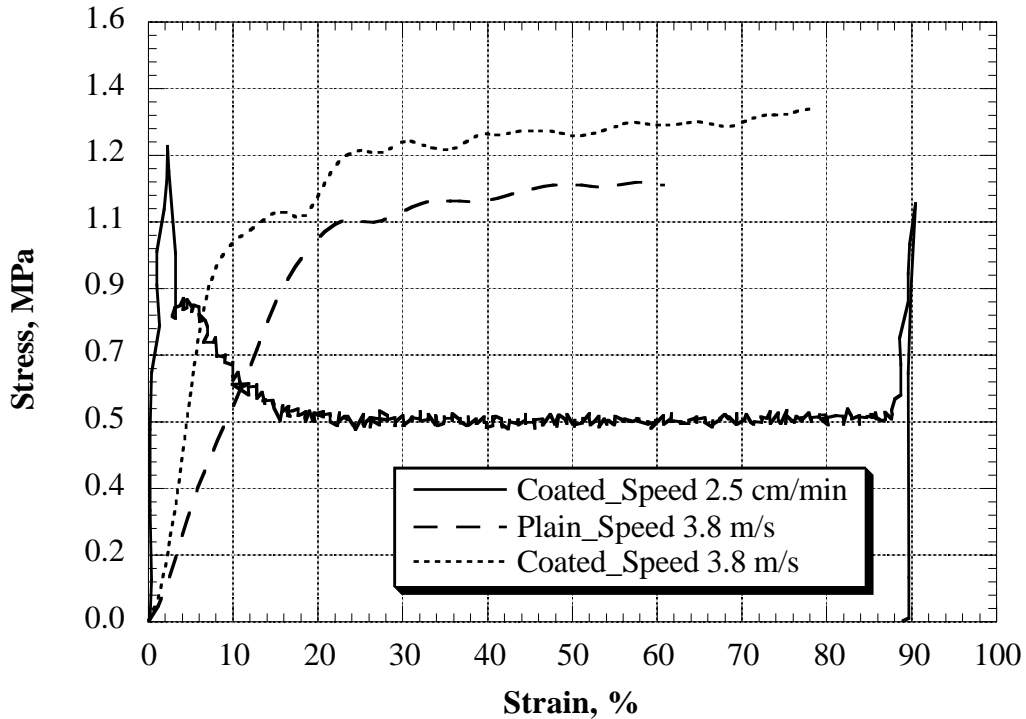


Fig. 8 - Penetration test results for carbon foam typical of the material used in the fabrication of cellular sphere 4a. All tests were performed with a 25.4mm flat face indenter. The coating used was similar to the one used on the cellular sphere cores. Note that dynamic tests were not performed to full specimen stroke capacity to avoid instrumentation damage through over-ranging.

Some interesting features about the response of carbon foam, which are highlighted in Figure 8, include an apparent sustained dynamic crush strength increase due to surface coating, and a large difference in sustained crush strength between static and dynamic loading cases. This curious behavior was identified by Kellas¹⁰, and was attributed to the test method and not material strain-rate sensitivity. It was postulated that the coating fills up the surface pores of the brittle carbon foam, enabling the entire surface layer of carbon ligaments to bear an equal share of the load and hence reach pure material strength levels. When the surface coating fractures, its effect on subsequent virgin layers of carbon ligaments depends on the speed of loading as shown in Figure 8. At slow speeds, the effect of the coating extends only as far into the foam as the coating's thickness. However, at high speeds the stress-relieving effect of the coating is felt by all carbon ligaments as long as the indenter travels fast enough to keep the layer of coating and/or carbon-foam debris trapped between a layer of virgin pores and the indenter face. The difference in dynamic sustained strength between plain and coated samples is

thought to be due to the fact that trapped debris alone is not as efficient a load distributor as the compliant coating. The cores of cellular sphere 4b were also of carbon foam, however, the foam was produced by a more cost effective fabrication process which resulted in poorer material quality, and undesirable density and strength gradient (lower surface strength). However, for similar material densities, the two types of carbon foam produced the same crush response.

Cellular Sphere Impact Tests

Five composite cellular spheres were fabricated and dynamically tested. Geometric details for the cellular samples, CV and OS are summarized in Table 5. Mass breakdown, instrumentation, and method of acceleration to impact speeds are summarized in Table 6. The two sample configurations used in the tests are shown schematically in Figure 9.

Table 5: Cellular Sphere and Sample Container Geometric Parameters and Materials

Spec. No.	Cell. Sphr. OD mm	Cell. Sphr. ID Mm	Cell Depth mm	OS OD mm	CV Thick.* mm	OS/CV Origin	OS Shape & Materials	CV Shape & Material
1	317.2	180.1	66	152.4	5.61	LaRC/ LaRC	Hemisphere Bismuth filled 3mm thick Alum. Shell	Hemisphere Loose Plies of Ks
2	315.0	176.0	66	152.4	5.45	LaRC/ LaRC	Hemisphere Bismuth filled 3mm thick Alum. Shell	Hemisphere Loose Plies of Ks
3	317.2	180.1	66	152.4	5.45	LaRC/ LaRC	Hemisphere Bismuth filled 3mm thick Alum. Shell	Hemisphere Loose Plies of Ks
4a	308.9 [†]	168.6	64	160.4	2.35	JPL**/ LaRC	Spherical Canister Alum. & Polyur. Foam	Hemisphere Ks
4b	308.0	171.5	64	155.0	5.45	JPL**/ LaRC	Spherical Canister Aluminum	Hemisphere Ks

* Thickness measurements were taken with the kevlar pile being finger tight compressed.

[†] Excluding the thickness of the loose kevlar plies.

** Includes self-contained data IES 50-series data recorder with three accelerometers.

Table 6: Mass Breakdown and Impact Parameters

Spec. No.	Sphere Mass kg	OS Mass kg	CV Mass kg	Total [†] Mass kg	Test Method	Impact ^{††} Vel. m/s	Impact [‡] Attitude Degrees	Data Acquisition/ Instrumentation
1	1.534	3.686	0.215	9.85	Free-Fall Dart	32.0	4-6	16 bit A/D @ 50 kHz via umbilical / Back-plate* & OS accelerometers
2	1.279	3.650	0.189	9.30	Free-Fall Dart	30.3	5-7	16 bit A/D @ 50 kHz via umbilical / Back plate* & OS accelerometers
3	1.703	3.510	0.189	12.38	Bungee Accel.	35.5	2-3	16 bit A/D @ 50 kHz via umbilical / Back-plate*, OS** & Vel. meas. accel.
4a	1.996 +0.245 Ks	2.402	0.079	14.47	Bungee Accel.	42.3	9-11	16 bit A/D @ 5 kHz via umbilical / Back-plate*, OS, & Vel. meas. accel.
4b	2.015	3.774	0.124	14.31	Bungee Accel.	40.4	2-3	12 bit A/D @ 118 kHz IES Recorder / Back-plate*, OS & Vel. meas. accel.

[†] Total mass includes ballast (or fins for free-fall), instrumentation and packaging material mass.

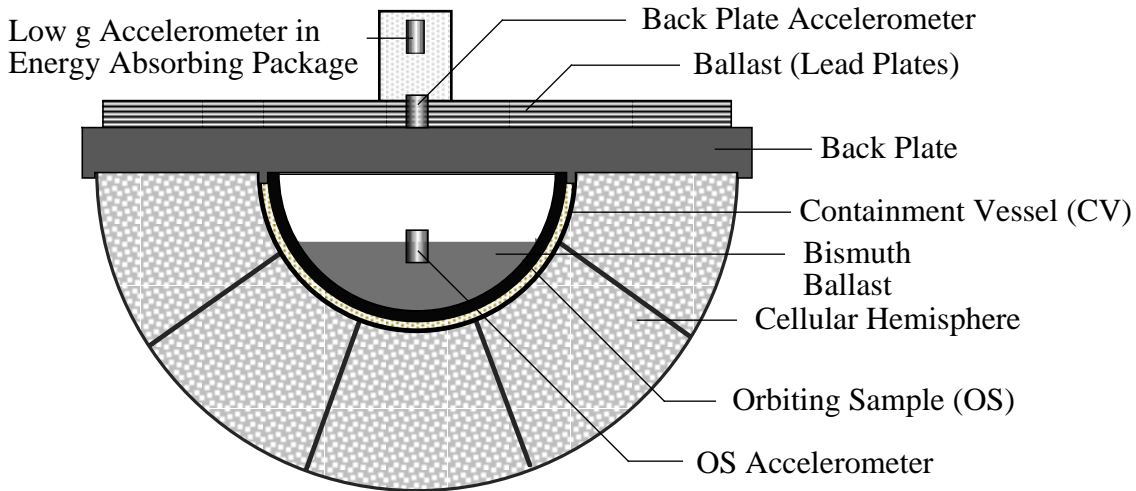
* Bakelite plate rigidly attached to cellular sphere.

^{††} For spheres 3, 4a, and 4b the velocity was measured by integration of a high sensitivity accelerometer. For spheres 1 and 2 the velocity was estimated from video.

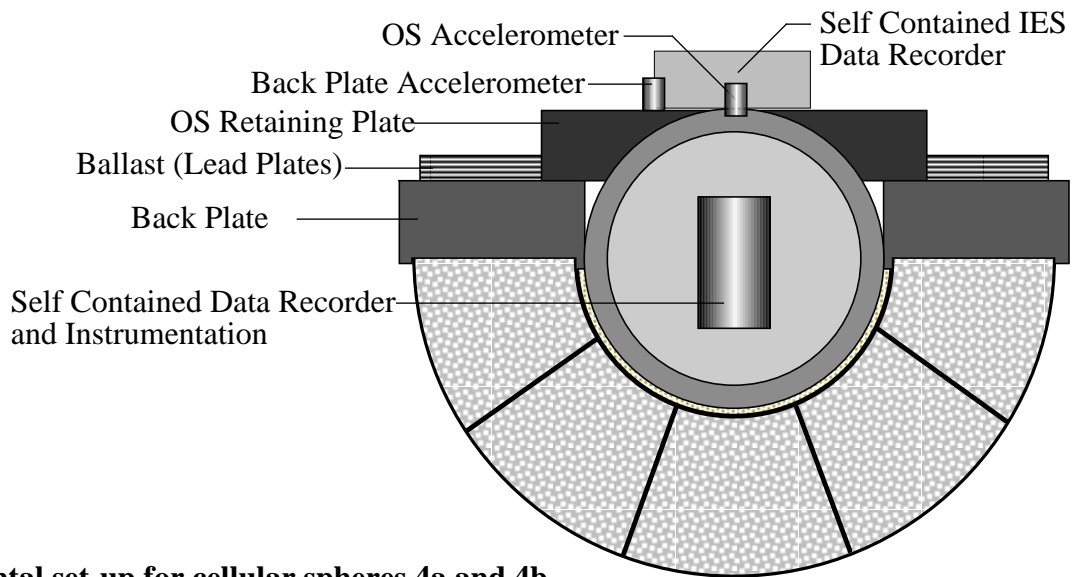
** OS Acceleration data was lost due to data cable failure.

[‡] Impact attitude was estimated roughly from video and/or permanent deformation.

Typically the test assembly (see Figure 9) consisted of a hemispherical composite cellular sample attached rigidly to a back plate (bakelite), a surrogate containment vessel (CV) hemispherical in shape, a surrogate (or actual) orbiting sample (OS), and a data acquisition system and instrumentation.



(a) Experimental set-up for cellular spheres 1, 2 and 3.



(b) Experimental set-up for cellular spheres 4a and 4b.

Fig. 9 - Experimental set-up for dynamic cellular sphere tests. Each back-plate contained a 3mm-deep machined channel to accept the base of the cellular sphere, which was secured in place using polyester filler.

For the first two tests, a free-fall method was used to accelerate spheres 1 and 2 to impact speed. This method involved the specimen set-up shown in Figure 9(a) with the addition of a set of three lightweight fins attached to the back plate. The complete assembly was dropped from a height of 70.87 m off a 73 m tall gantry structure located at the Full Scale Impact Dynamics Research Facility of NASA Langley Research Center (LaRC). A photograph of the first drop-test is shown in Figure 10. For this series of

tests, an umbilical chord was used to transmit the data to a personal computer, which was located at the top of the gantry. Data from two accelerometers were acquired with a 16-bit resolution at a rate of 50 kHz. For the first two tests, the “low-G” accelerometer and cushioning package, shown in Figure 9(a), were not used. Instead, the velocity was estimated from digital video by measuring the drop distance during the last two whole frames and dividing by the time interval between frames.



(a) Cellular sphere 1 during free-fall.



(b) Cellular sphere 1 following drop test.

Fig. 10 - Photographs from the drop test of cellular sphere 1. (a) Free-falling cellular sphere assembly is shown in the center of photograph, and (b) the cellular sphere shown resting on the ground after the drop test. Note that the effectiveness of the fins to align the sample with the vertical improves with increasing velocity. Typically the attitude at impact was maintained within 6° -off vertical despite the presence of gusty winds and umbilical cord.

Because of the high drag of the free-fall specimen assemblies, which limited the impact speeds, a custom accelerator was designed and used in cellular sphere 3, 4a and 4b tests. A simplified schematic of the accelerator system is shown in Figure 11. The system consisted of a set of two 19-mm-diameter, 50-m-long bungee cords which were stretched between the ground and the top center beam (partly visible in Figure 10) of the gantry structure. Note that for clarity, only one of the two planes of bungee cord is shown in Figure 11, though the actual system in its final configuration consisted of two perpendicular vertical planes of bungee cords.

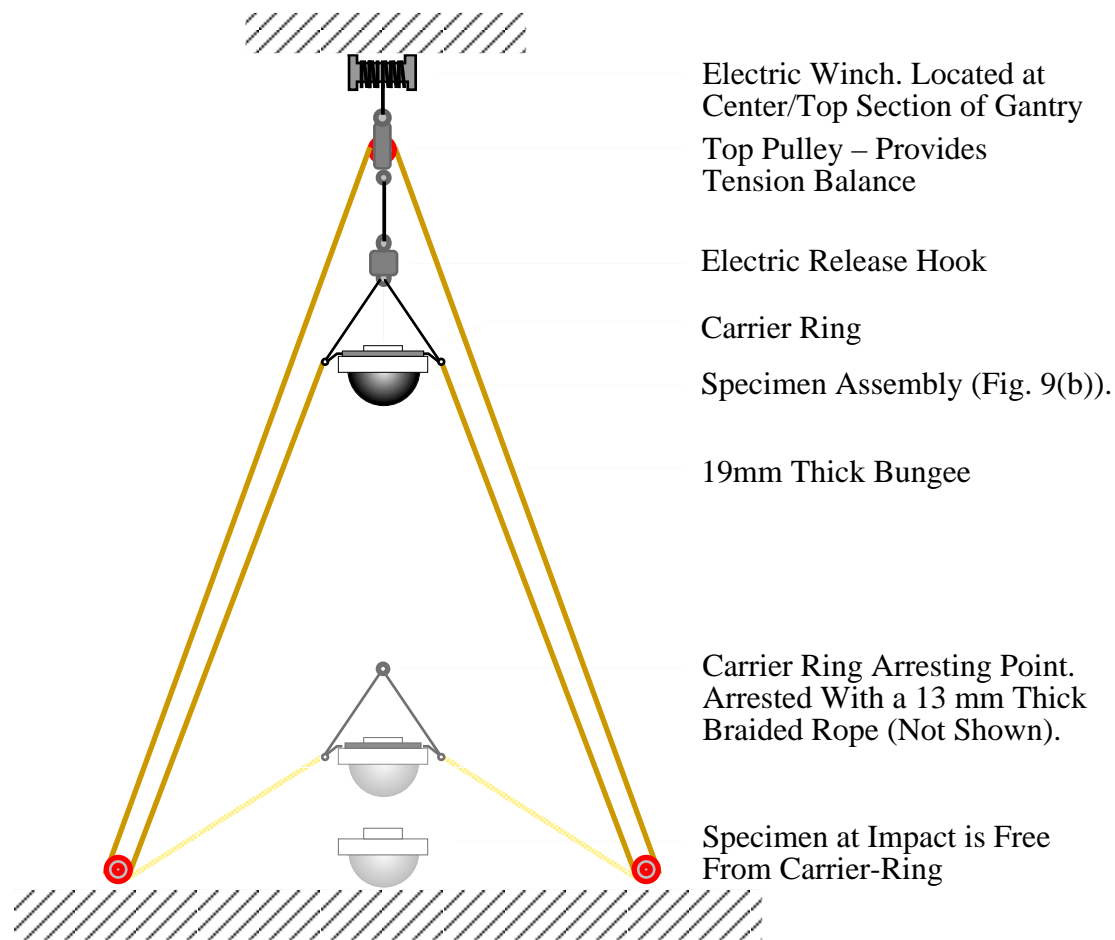


Fig. 11 - Schematic of bungee accelerator facility used for the last three cellular sphere tests. Only one plane of bungee cord system is shown, though the actual accelerator system consisted of two bungee cords in perpendicular vertical planes.

Basic features of the catapult system include an electric winch (attached to the top of the gantry), a tension-equilibrating double-pulley block at the top, four ground-mounted pulley blocks, an electric release hook, a specimen carrier ring and strap harness, and a carrier ring arresting device consisting of a braided nylon rope. A multifunctional friction drag device was also used to (a) limit initial accelerations to a given maximum, typically within the range of the low-G accelerometer which was used for impact velocity calculation, and (b) to hold the specimen in contact with the harness during bungee pull-back and hold stages. Limiting the initial acceleration of the specimen assembly was also found useful in overcoming the sluggish response of the bungees at release, associated with their viscoelasticity and the inertia of the ground pulleys.

The impact velocity of a given specimen assembly was estimated with the aid of a custom computer program which combined geometric and mass details with empirical data of bungee and arrest rope responses to predict impact velocities and various system component loads. The computer simulation proved to be a valuable tool in estimating bungee strain, arrest rope loading, maximum winch loading,

and incremental impact velocity changes for a given family of specimens. However, due to the drag coefficient uncertainty of the combined accelerated mass, including the bungees themselves, surrogate specimens of equal mass and projected area were used prior to actual testing to verify estimated velocities. Typical velocity calibration specimens included stiff water-filled balloons mounted on plywood back-plates with appropriate instrumentation to calculate the impact velocity. A photograph of an actual cellular sphere sample during its acceleration towards the ground is shown in Figure 12.



Fig. 12 - Photograph of a catapulted cellular sphere sample. One of six legs of the 73-m-tall gantry of impact dynamics research facility at NASA LaRC is shown in the background.

Typical back-plate and OS acceleration time responses for the free-fall test case are shown for cellular sphere 2 in Figure 13, and for the catapulted sphere 4b in Figure 14. Instrumentation and other test-related parameters can be found in Table 6, and the specimen set-up and relative positioning of the instrumentation are shown in Figures 9(a) & (b) for cellular sphere 2 and 4b respectively. Note that a low-G accelerometer was not used in the cellular sphere-2 test, and the velocity at impact was estimated from the digital video.

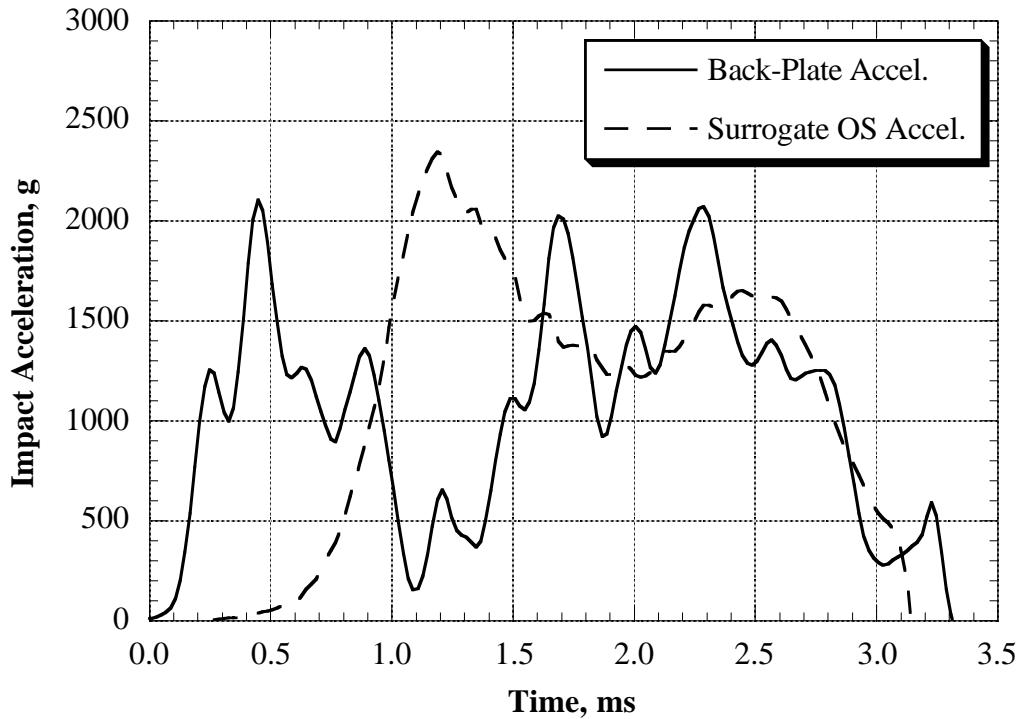


Fig. 13 - Acceleration time responses for cellular sphere 2. Total impact mass = 9.30 kg, impact velocity = 30.3 m/s, attitude at impact approximately 6°. Data were acquired at 50 kHz and filtered at 5 kHz using a low-pass filter.

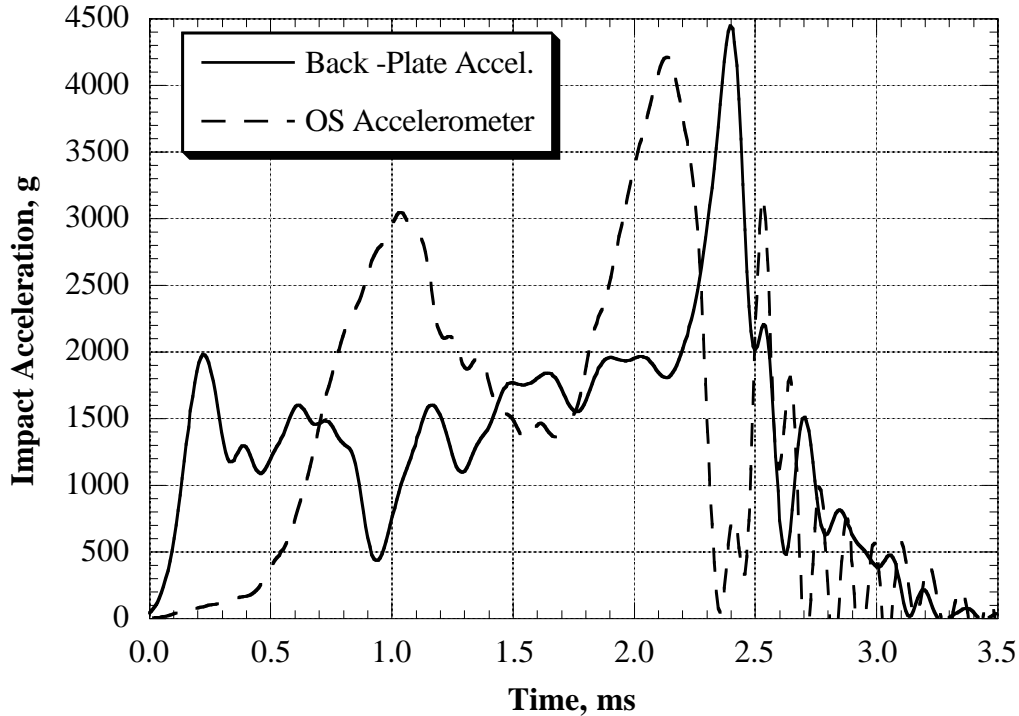


Fig. 14 - Acceleration time responses for cellular sphere 4b. Impact mass = 14.31 kg, impact velocity = 40.4 m/s, attitude at impact approximately 2.5°. Data were acquired at 118 kHz and filtered at 5 kHz using a low-pass filter.

Despite differences between test samples such as constituent materials, impact velocity, and total mass, the corresponding acceleration responses for the two tests were very similar. Typically acceleration responses from all test cases were characterized by a time shift in the OS response compared to the back-plate acceleration, thought to be associated with the flexible CV which separated the OS from the cellular sphere's inner cup. The apparent decoupling of the OS from the cellular sphere was also responsible for the subsequent oscillation of the OS within the cellular sphere, which lead to acceleration extremes every time the OS came in contact with either the cellular sphere's inner cup (fully compressed CV) or the back-plate. Depending on the impact velocity, relative OS-to-sphere mass ratio, and damping characteristics of the CV, the OS exhibited several acceleration extremes during the impact. In Figure 13, for example, the OS appears to have made contact with the cellular sphere's inner cup at $t=1.2\text{ms}$. A similar but more complex series of events is also evident in Figure 14 where due to the higher energies involved, the OS appears to have made contact with the inner cup and the back plate. In order to obtain a better understanding of the oscillation response of the OS within the cavity of sphere 4b, the relative velocity of the OS with respect to the back plate was determined by integration and presented in Figure 15 together with the accelerations.

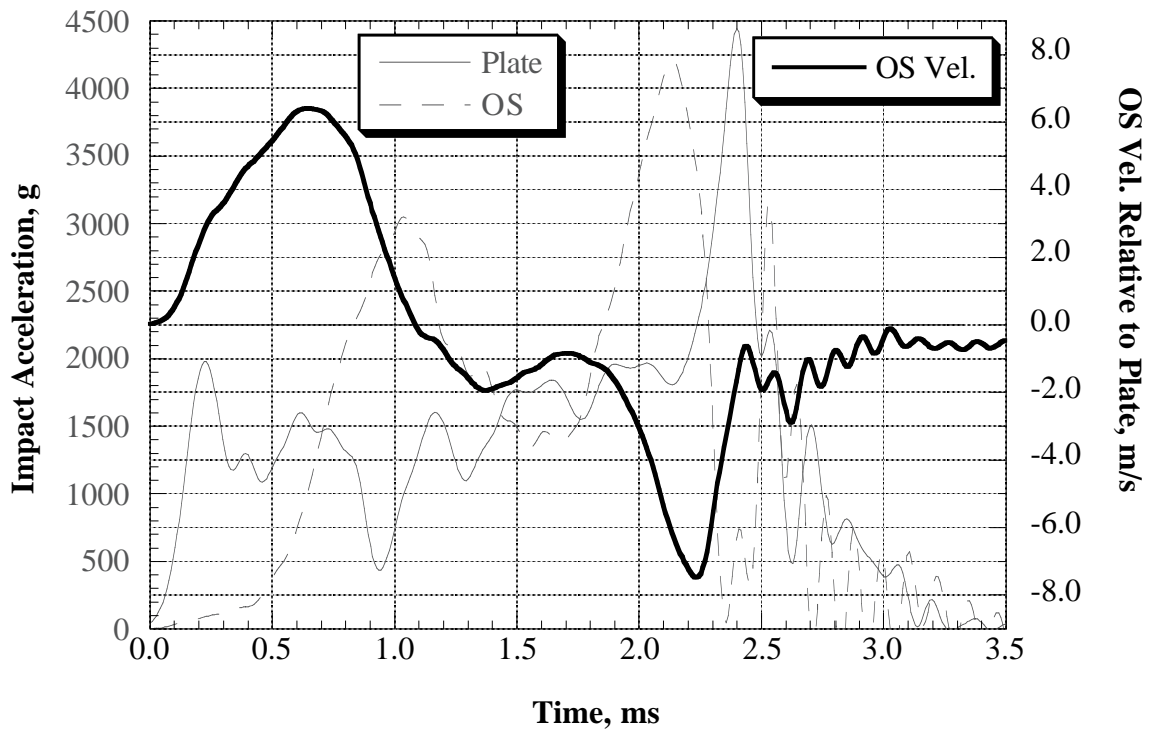


Fig.15 - OS velocity relative to the back plate. Downward travel (towards the spherical inner cup) is indicated by positive velocity values.

The relative velocity response of Figure 15 shows that, at impact, the OS travels toward the sphere's inner cup as the CV is being fully compressed after approximately 1.0ms and before the relative velocity

vector reverses direction. At approximately 1.7 ms, the OS relative motion appears to be constrained momentarily, perhaps by the downward flexing of the back plate and/or buckling of the inner cup, before its upward acceleration and impact with the back-plate at approximately 2.4ms.

A suspected secondary mass decoupling within the OS following its impact with the back plate was thought to be responsible for the induced high-frequency vibration. This high frequency vibration was recorded by both external and internal data acquisition systems as shown in Figure 16.

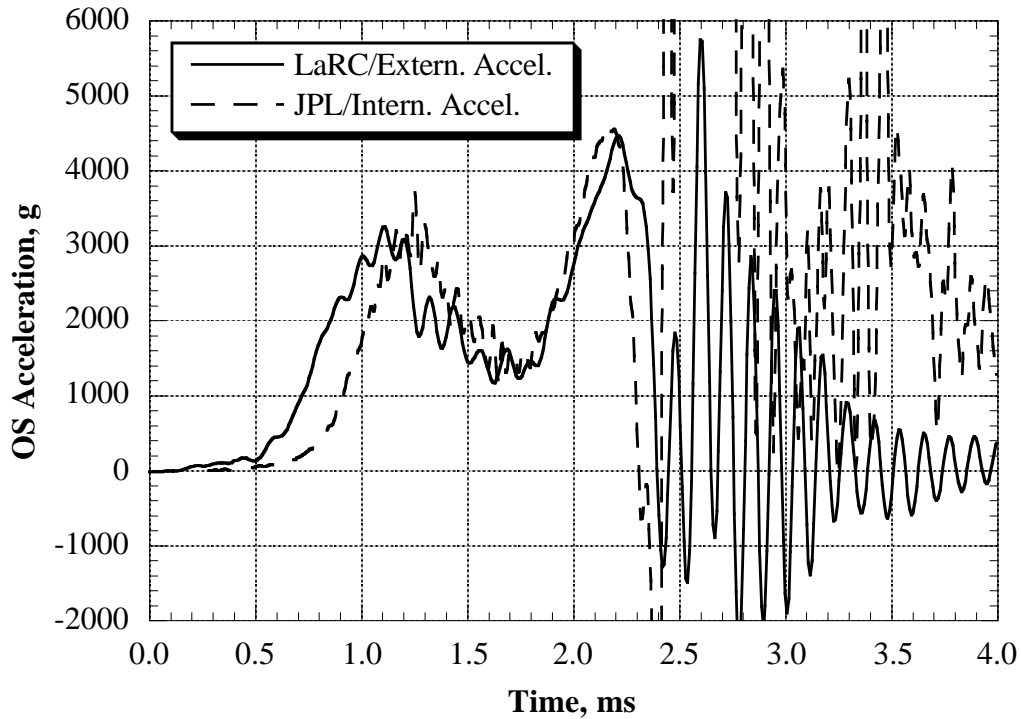


Fig. 16 - Comparison of external and internal OS mounted accelerometer responses for cellular sphere 4b. No filtering was applied to the data. Note that while the externally measured vibration, which initiated at approximately 2.5 ms, eventually settled to zero, the internally measured one did not, indicating perhaps an internal instrumentation failure due to resonance or conductor breakage.

While the actual cause of the mass decoupling within the OS is not known, it is highly probable that excessive movement of the internal data acquisition package and eventual contact with the OS interior wall was responsible for the induced vibration. Supporting evidence for excessive internal package relative motion is shown in Figure 16 through a 0.2ms initial time delay between the external and internal acceleration responses. It is worth noting at this point that the large dynamic loads experienced by the OS following its impact with the back plate are unique to the particular test set-up used since the actual energy absorber would extend all the way around the OS.

Obvious differences between the two cases presented in Figures 13 and 14 include back-plate acceleration peaks unique to each test case such as the back-plate acceleration response of sphere 2 which contains a double and relatively high initial peak as compared to sphere 4b. Another difference is the relatively high peak observed at the end of the back-plate acceleration response of sphere 4b as compared to sphere 2. While these differences could be attributed to factors such as impact attitude, and/or bottoming out of sphere 4b, examination of the data from a different perspective is required before a firm conclusion can be made. Such alternative perspective includes the examination of the crush response of the spheres without the superimposed effect of the OS oscillation. In other words, how would the cellular sphere acceleration response, A_{av} , look like if the OS was fully coupled to the rest of the structure? To answer such a question a simple free-body diagram approach (see Figure 17) was adopted in conjunction with the following assumptions:

- (a) Accelerations measured at the back plate (Figure 17(b)) are the same as those at the cg (center of gravity). In effect this implies that the back plate remains rigidly attached to the impact sphere for the full duration of the impact, and that the cg position is unaffected by the crushing of the sphere. Moreover, this implies that there are no significant rotations during crushing.
- (b) Accelerations measured at the top of the OS (Figure 17(c)) are the same as those at the cg. Again this implies that the cg position remains fixed with respect to the OS original geometry.
- (c) The entire system mass is conserved during the crushing process; i.e., the mass of any fractured pieces or poorly mounted components that are ejected clear from the system during impact have no significant effect on the total mass.

Force equilibrium for each of the cases of Figure 17 yield the following relationships.

$$F_c = A_{av}M_{tot} , \quad (1)$$

$$F_c - F_{cv} = A_sM_s , \quad (2)$$

$$F_{cv} = A_{os}M_{os} \quad (3)$$

Simultaneous solution of 1-3 lead to:

$$A_{av} = \frac{A_sM_s + A_{os}M_{os}}{M_{tot}} \quad (4)$$

Using Equation 4 in conjunction with the measured back-plate and OS accelerations, average acceleration responses for cellular sphere 2 and 4b were derived and presented in Figure 18. Average acceleration/time response reflects more accurately the crushing characteristics of the cellular sphere,

thus allowing a more accurate assessment of factors such as crush initiation, sustained crush load and crush stroke capacity to be made.

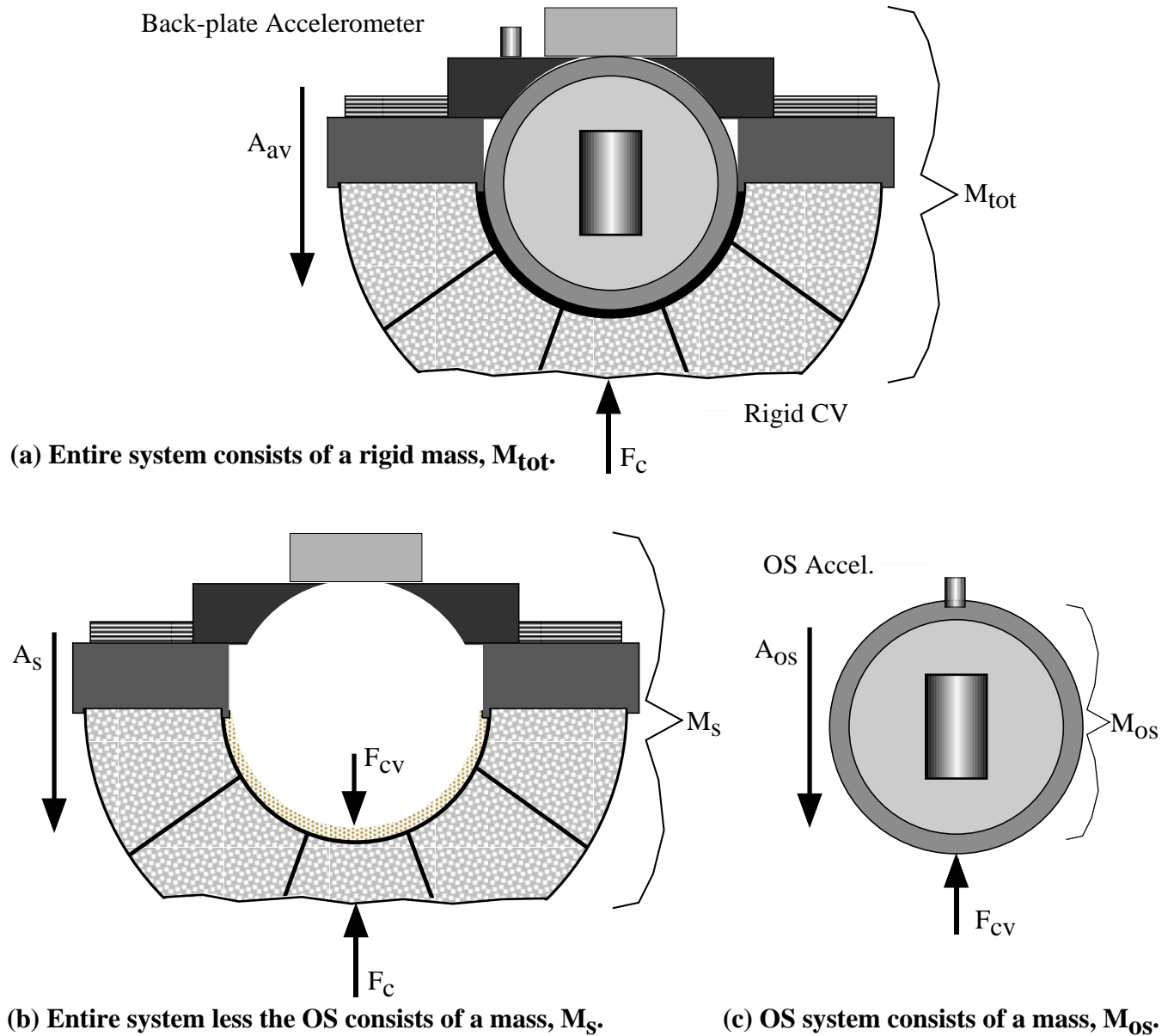


Fig. 17 – Free-body diagrams for cellular sphere test assembly during impact. In (a) the OS is assumed to be fully coupled to the rest of the system of total mass M_{tot} , (b) the cellular sphere plus back-plate and instrumentation make-up the mass M_s , and (c) the OS and its subcomponents make up the mass M_{os} .

Figure 18 shows much less difference between the averaged acceleration response of sphere 2 and 4b than was seen in Figures 13 and 14, indicating that the large differences were indeed a byproduct of the OS oscillation rather than a genuine structural feature of the cellular sphere response. To the contrary, the large back-plate acceleration peak seen at the end of the impact response of sphere 4b (Figure 14) is still evident in Figure 18, which indicates that perhaps sphere 4b had reached its stroke capacity.

Although not entirely clear from Figure 18, it is possible that the double peak in the initial average-acceleration response of sphere 2 is a crush-related feature associated with the relatively large impact attitude. Progressive, rather than simultaneous, engagement of the cell wall junctions would indeed lead to such a crush initiation response. A further plausible cause, which may be solely or partly responsible for the observed response, is partial loss of impact mass due to fin separation.

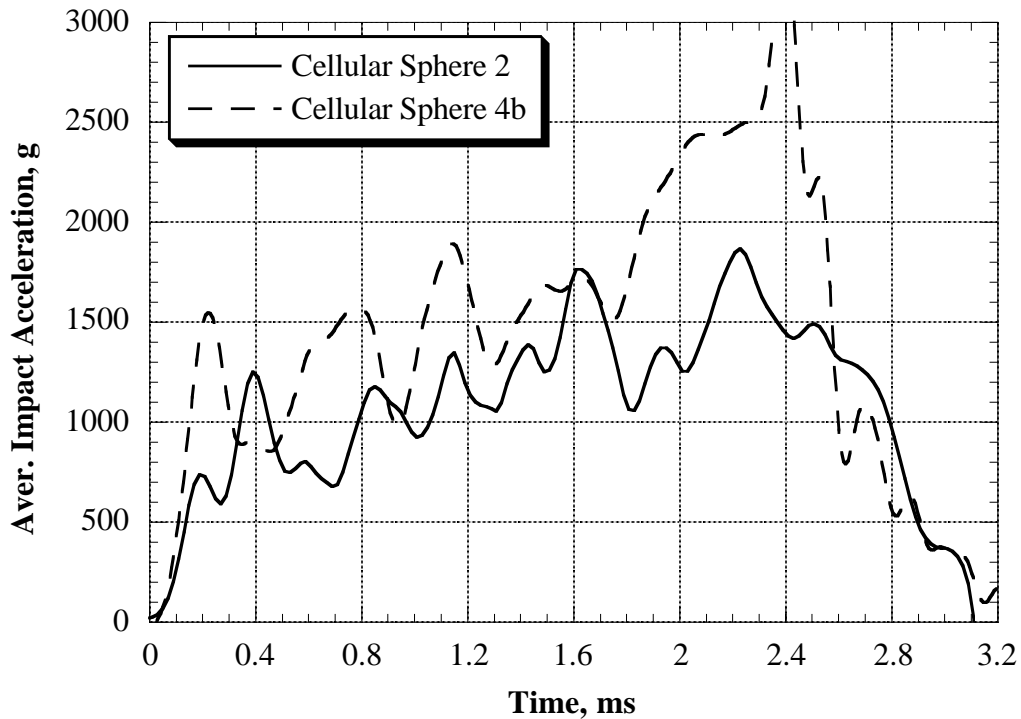


Fig. 18 - Average acceleration/time responses for cellular spheres 2 and 4b. Data were generated using equation 4 in conjunction with the raw acceleration responses of Figures 13 and 14. Data were filtered using a 5 kHz low-pass filter.

Often, a more useful way for visualizing the crush response of energy absorbers is load/displacement or load/strain plots. For the cellular spheres these types of responses can be generated from the average-acceleration time history data. Crush load is obtained by multiplying the average acceleration by the total mass and crush displacement is obtained by double integration of the average acceleration. Such an example is shown in Figure 19 for the crush response of cellular sphere 4b. For this example, the crush stroke percentage was obtained by dividing the displacement by the core depth of 64mm. In other words, the incompressible thickness of the inner and outer spherical shells was neglected from the cellular sphere total crushable depth.

Features worth noting in Figure 19 include a relatively rectangular pulse and large crush stroke, indicative of a near-ideal crush response. Also shown in Figure 19 is additional supporting evidence of

the fact that sphere 4b has reached its stroke capacity at about 90%. Bearing in mind that most crushable energy absorbers are only capable of approximately 80% stroke³⁻⁹, the cellular sphere concept exhibited an impressive performance. It is believed that the superior crush stroke of the cellular sphere concept is related in part to the excellent crush performance of the carbon-foam core and the spherical nature of the cellular structure which allows crushed material to be deflected away from the critical area.

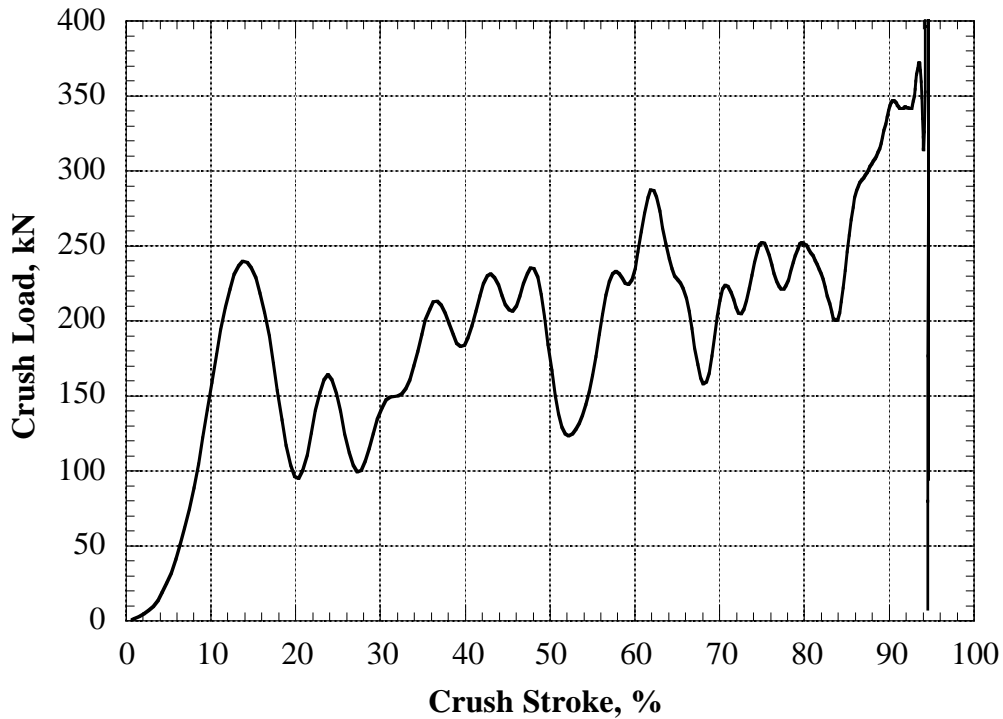


Fig. 19 - Crush load versus crush stroke for cellular sphere 4b. The crush load is based on the average acceleration shown in Figure 18.

Typical crush deformations of cellular spheres are shown in the photographs of Figures 20-22 for spheres 3, 4a and 4b respectively. The crush deformation shown in Figure 20 was typical of all cellular sphere samples except from cellular sphere 4a, which contained separate rather than co-cured kevlar containment and penetration resistant layers.

As anticipated, the separate outer kevlar shield of sphere 4a offered excellent containment. Furthermore, following the impact, the kevlar shield appeared to conform well around the crushed sphere without any signs of failures. However, the loss of effective coupling between the co-cured graphite shell and the cell webs had a detrimental effect on the crush initiation load as shown in Figure 23. Fragmentation of the graphite plies, shown in Figure 21, resulted in loss of lateral support to the cell webs and hence a lower crush initiation load. To the contrary, hybridized and co-cured kevlar layers in the outer shell exhibited sufficient post-crush integrity and thus maintained adequate lateral support to the cell-webs to constrict their folding into the “S” like mode shown in Figure 22. While it is generally accepted that a

deformation characterized by plastic-like wrinkling (Figure 20) as opposed to brittle fracture (Figure 21) dissipates energy more efficiently, it is believed that initial energy absorption deficit between samples 4a and 4b was caused primarily by the loss of lateral cell-web support and not by the poor energy dissipation in the outer shell itself.



Fig. 20 - Post-crush photograph of cellular sphere 3. Plastic-like wrinkling in the kevlar layers and lack of fabric fractures are indicative of good post crush integrity and perhaps good penetration resistance.



Fig. 21 - Post-crush photograph of cellular sphere 4a and its kevlar 29 penetration shield, which was removed after impact. The estimated off-vertical angle was 10°.

Examination of the average acceleration/time and load/stroke response of sample 4b indicated that even though the energy absorber had almost exceeded its stroke capacity of approximately 90%, the dynamic loads were maintained well within the 3500g design requirement as shown in Figure 18.



(a) Cellular Sphere 2 – Polyurethane foam core.



(b) Cellular sphere 4b– Carbon foam core.

Fig. 22 - Cross-section view of crush deformation for cellular spheres 2 and 4b. In both cases the co-cured hybrid shell maintained adequate lateral support to the cell-webs to promote the “S” like folding.

However, the irregular crush load characteristics of sphere 4a, coupled with a higher impact speed which resulted in 10.8% higher impact energy compared to 4b, lead to an impact acceleration peak of 5000g. As a result of energy absorber “bottoming-out,” inner spherical shell damage was evident in both samples 4a and 4b with the cup of sample 4a being more severely damaged. It is believed that the inner spherical shell fracture of sphere 4a was primarily responsible for the superficial OS damage observed in the external polyurethane foam cover of the OS as shown in Figure 24. In addition to the “H” shape crack shown in Figure 24, the foam cover contained a pentagonal impression caused by the stress concentration of the cell-webs. Closer inspection of the OS by JPL personnel revealed no damage of the sample container part of the OS.

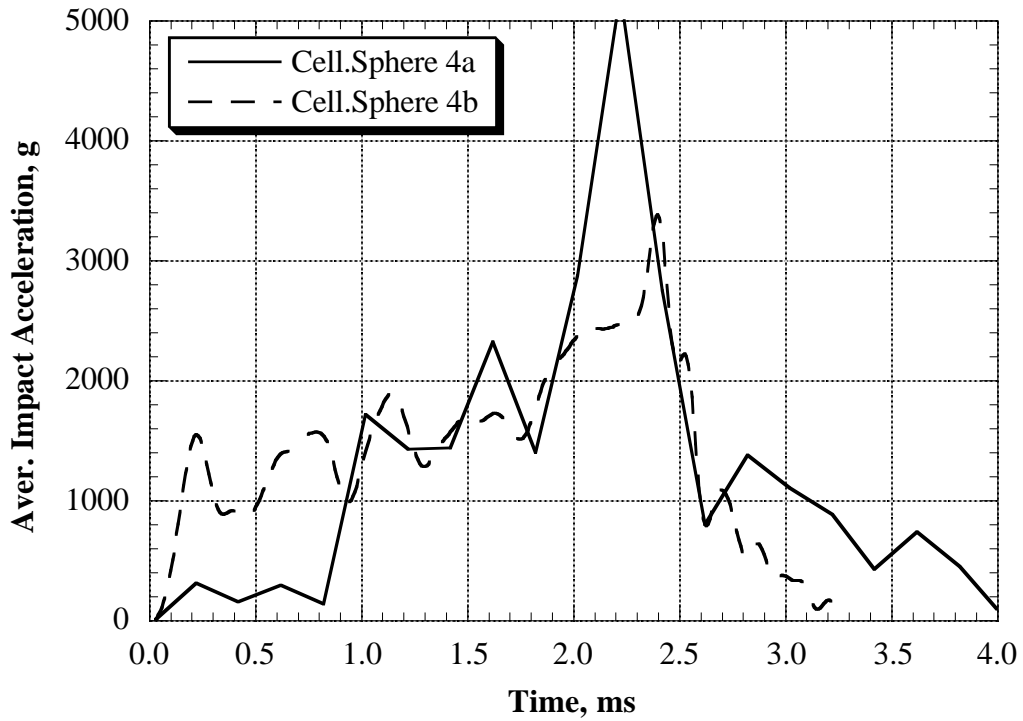


Fig. 23 - Average acceleration responses for cellular spheres 4a and 4b. The only structural difference between the two samples was the separate kevlar shield in 4a instead of the co-cured kevlar shield in 4b.



Fig. 24 - Post-impact photograph of the OS used in the cellular sphere 4a. This particular OS consisted of a spherical container covered externally by high-density polyurethane foam. The damage shown is limited to the outer foam cover of the OS.

“Y” Element Tests

Cylindrical samples, containing a single “Y” intersection, were removed from each of the first three cellular spheres following impact testing. Specimens were removed from virgin areas of the sphere samples as shown in Figure 25a. Specimen removal from spheres 4a and 4b was not possible due to the more severe impact conditions spheres 4a and 4b were subjected to, typically more than twice the impact energy and 20-25% more crushing than spheres 1-3.

Specimen preparation included filling of the concave face of each sample with polyester filler to create a flat base, and wrapping of the cylindrical surface with kevlar tape to simulate the radial (sample axis) constraint that the cell webs were subjected to in the cellular sphere. Without the kevlar-tape overwrap the foam core segments would simply disbond from the cell walls and provide no stability nor constraint during the crush process. The kevlar tape was secured in place using a spray tack adhesive. It was assumed that the flexible tape wrap had no direct effect on the crush loads. Because of the proximity of samples to each other, two out of four samples per sphere had their axis oriented at a small angle (5-10°) to the vertical.



(a) Bisected post-impact cellular sphere 2



(b) “Y” element sample

Fig. 25 - Photograph of cellular sphere showing the perforated areas from where the “Y” elements were removed. An imperfection in the expanded polyurethane foam core is shown on the bottom of the “Y” element sample adjacent to the cell wall. Each sample was 73.15 mm in diameter and approximately 70 mm tall.

All samples were crushed quasi-statically at speeds of 50.8 cm/min. Typical crush load/stroke responses are shown in Figure 26 for samples from sphere 1. Features worth noting include a relatively flat crush response for both axial and off-axis samples up to approximately 50% crush, and a slightly higher crush initiation load compared to the average sustained crush load values. The sustained crushing load measured within the initial stages (up to 40-50% stroke) of crush is thought to be an accurate representation of the “Y” element's response. However, as the constraining effect of the kevlar overwrap increases with increasing stroke, an artificial strengthening is thought to be occurring. As a result, the “Y”-element samples appear to bottom-out prematurely.

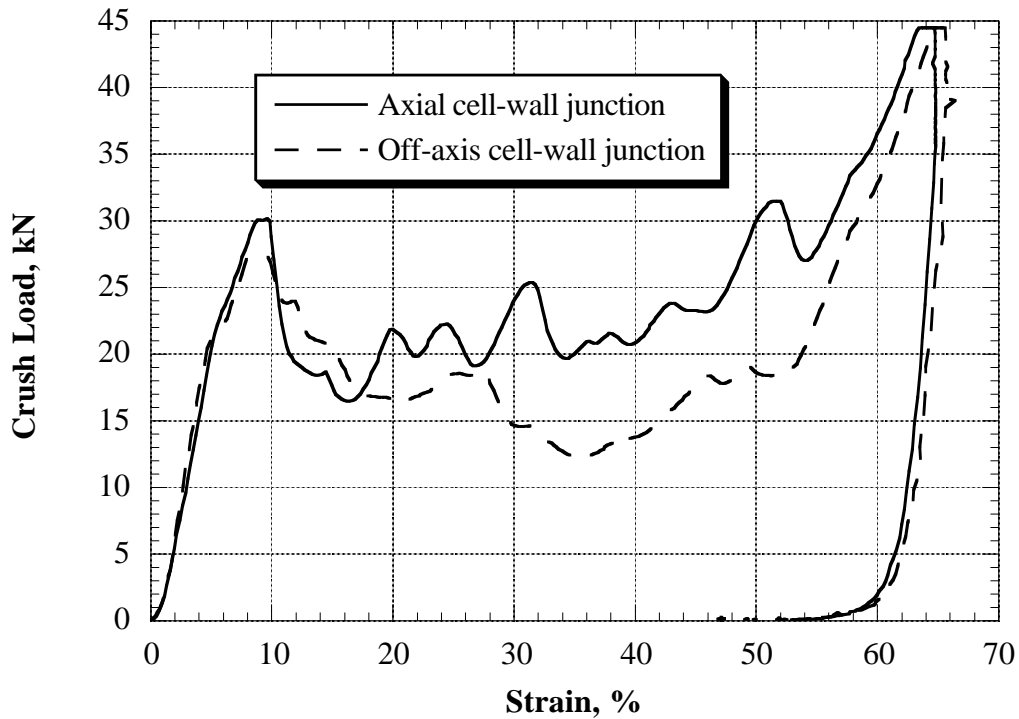


Fig. 26 - Typical crush responses of “Y” element samples removed from cellular sphere 1.

The crush initiation load is usually related to the imperfection sensitivity of a given specimen and for the “Y” elements was found to vary from 0 to 50% above the mean sustained crushing load value. It is worth noting that the magnitude of crush initiation load often regulates the subsequent mode of collapse. Typically, the off-axis samples exhibited a slightly lower crush initiation load as well as lower sustained crushing load due to the poorer stability. Due to lack of shear stability, which is an artifact of the off-axis test samples, progressive crushing in off-axis samples was often interrupted as shown in Figure 26 (approximately 30%). Note that such behavior is not typical of an off-axis element within the cellular sphere where shear stability is provided and sustained by the surrounding cells and foam core.

Theoretical Crush Load Determination

Sizing of the cellular structure was accomplished with the aid of a theory⁵⁻⁹ originally developed to describe the crush response of plastically deformed thin metal box structures and/or intersecting flange elements such as angles and cruciforms. In particular, the approach used by Wierzbicki⁶ to analyze metal honeycomb structures was the most relevant. The theory was modified appropriately to account for the foam core and laminated construction of the composite cellular structure. The main challenge in the application of the theory was found to be the selection and measurement of the appropriate input parameters, which for the laminated composite cell walls was not as straightforward as in ductile metals. In similar work involving thin composite cell walls³, measured tensile cell wall properties were used

successfully to determine effective yield stress values required by the analysis and the same technique was adopted herein.

In addition to the usual assumptions that are required for the formulation of the theoretical solution⁵⁻⁹, the following assumptions were also employed here for the theoretical prediction of the sustained crushing load:

- (a) The composite cell walls deform quasi-plastically in bending. The cell-wall effective yield stress is assumed to be 70% of the tensile ultimate-strength³ measured on flat coupon specimens, for each cellular sphere architecture. Since for the same number of plies the flat coupon specimen thickness was somewhat lower than the measured cell wall thickness, as reported in Table 3, the effective yield stress was adjusted accordingly to correspond to the measured cellular sphere cell wall thickness.
- (b) Composite cell walls are treated as quasi-isotropic.
- (c) Ply delamination does not dissipate a significant amount of energy compared to other failure modes and therefore it is neglected.
- (d) The resistance imposed by the foam core on the folding flanges is uniform throughout the folding process and foam/skin disbond is neglected. Moreover, the foam is assumed to be isotropic.
- (e) For low-density foam core, lateral expansion of the foam during crushing is neglected (i.e., zero Poisson's ratio). This assumption while irrelevant for carbon foam is needed for the case of polyurethane core where a significant lateral expansion was possible during crushing.
- (f) The conical cells are treated as cylindrical. This has two implications; first, the cell walls are rectangular instead of trapezoidal, and second the plane of the cell walls is parallel to the loading direction.
- (g) The crush load calculation is based on the engagement of a fixed number of intersections. As a result, the theoretical load prediction is only applicable to the initial stages of crushing.
- (h) The crushing load contribution due to the strength of the outer shell is neglected.

Although the “soccer ball” approach was adopted in the fabrication of all cellular spheres, a general theoretical approach was developed to allow for analytical examination of other sphere-sectioning options and in particular the sixty triangular cell case.

In accordance with the original theoretical procedures⁴⁻⁹, a cross section of the cellular structure normal to the loading direction is treated as being composed of a given number of characteristic elements depending on the geometric make-up of the sphere. The crush load for the characteristic element is determined using a total energy balance approach. The crush load for the cellular sphere is then determined according to the total number of elements engaged during the initial stages of the impact event. In the case of the “soccer ball” approach, the characteristic element is a “Y” formed at the cell wall intersections such as point “a” shown in Figure 2, with flange length equal to the chord $ab/2 =$

0.2068R, where R is the sphere radius. In this case it is assumed that five elements (“a”, “b”, “c”, “d” and “e”, see Figure 2) will be engaged if impact occurs in the vicinity of point “O”. In fact it can be shown using simple geometry that for an axial impact at point “O”, the five “Y” elements are the only elements engaged for a crush distance up to approximately 0.28R, which for the geometry of spheres used in this study, corresponds to approximately 67% stroke. While the number of active elements remains uniform in the range between 0-67% stroke, the corresponding crush load is not. Since the engagement length of webs such as “ag” is a function of the crush stroke, the area of core material engaged during the crush process is also a function of the crush stroke. Therefore, only an estimate of the initial crush load can be made based on the integrated contribution of the five elements (“a”, “b”, “c”, “d” and “e”), where the maximum applicable crush displacement ($=0.1541R$) is determined based on the crush front just contacting point “g”. Note that if impact occurs at point “B”, which represents a 37° off-axis impact from point “O”, six “Y” elements would be engaged. The crush load can be estimated for this case, as before, by summing up the contribution of the six elements.

If the cellular sphere were to be constructed of sixty isosceles triangles, two characteristic elements need to be considered, a five-flange element such as the one at point “O” with flange length $O_f=0.2857R$, and a six-flange element such as the one at point “A” with flange length $A_f=0.3530R$. Both “ O_f ” and “ A_f ” represent a chord length. If impact occurs in the vicinity of point “O”, five six-flange elements (“A”, “B”, “C”, “D” and “E”) plus one five-flange element (“O”) would be engaged. However, unlike the soccer ball approach, where all five elements are engaged almost simultaneously, here the element at “O” is engaged first followed (~47% stroke later) by the five six-flange elements. Undoubtedly, this would lead to a less desirable crush response, containing a ramped-up, instead of a near-rectangular shaped, load/displacement response. A different combination of elements, but similar crush response is anticipated, if impact would occur in the proximity of point “B” where the six-flange element “B” is engaged first, followed by three six-flange elements (“A”, “C” and “G”), and the three five-flange elements (“F”, “H” and “O”).

Since all of the cases discussed above involve a characteristic element, which resembles a star with three, five or six flanges; a general theory was developed for an n-flange element where “n” is the number of flanges. This type of general treatment required, in addition to the previous assumptions, the following assumptions:

- (i) The flanges of the n-flange element are equally spaced thus forming an angle $2\psi = 360^\circ/n$, see Figure 27(a). This assumption is required for $n=3$, where the actual value of the angles between the flanges, measured in the plane normal to the element axis, are $\theta=124.3^\circ$ and $\phi=111.4^\circ$, with θ and ϕ defined in Figure 2.

- (j) The n-flange element consists of n “V” sub-elements each of angle 2ψ and flange thickness t , which delaminate locally at the flange intersection of the “Y” element during the folding process, as shown in Figure 27(b). This implies that no cell wall tearing is necessary for progressive crushing.
- (k) Finally, it is assumed that the total energy dissipated during plastic collapse of the “star” element consists of four distinct contributions:

- (a) Energy dissipated at the corner of each constituent “V” sub-element, through extensional deformation, denoted E_1 . The toroidal shell section formed during the deformation process⁵⁻⁹ is assumed to have a minor radius b , and the cell walls have a yield stress σ . The total energy in an n-flange element is given by:

$$E_1^{\text{tot}} = 4n\sigma t b H I_1 \quad (5)$$

where according to Wierzbicki⁶,

$$I_1^n = \frac{\pi}{(\pi - 2\psi)\tan\psi} \int_0^{\pi/2} \cos\alpha \left\{ \cos\psi - \cos\left(\psi + \frac{\pi - 2\psi}{\pi}\beta\right) \right\} d\alpha \quad (6)$$

and
$$\tan\beta = \frac{\tan\alpha}{\sin\psi} \quad (7)$$

- (b) Energy dissipated by moving horizontal hinges during flange folding (Figure 27), denoted E_2 . The total energy for n flanges of thickness $2t$ is given by:

$$E_2^{\text{tot}} = n\pi C_n \sigma t^2 \quad (8)$$

where C_n is twice the flange length of a “star” element, and for the soccer-ball sphere it is equal to the chord length “ab”, shown in Figure 2. For a soccer-ball sphere of radius R , C_n is given by:

$$C_3 = 2R \sin \left(\frac{\frac{\pi}{2}}{4 \sin \frac{\pi}{3} + \frac{1}{\tan \frac{\pi}{5}} + \frac{1}{\sin \frac{\pi}{5}} + 1} \right) \quad (9)$$

- (c) Energy dissipated by the inclined hinges in each “V” sub-element, denoted E_3 . Note that the fact that the composite properties for the inclined hinges are different than those of the horizontal hinges is neglected through the assumption of quasi-isotropy. The total energy for the n-flange element is given by:

$$E_3^{\text{tot}} = n\sigma t^2 \frac{H^2}{b} I_2^n \quad (10)$$

where according to Wierzbicki⁶, $I_2^n = \frac{1}{\tan \psi} \int_0^{\pi/2} \frac{\cos \alpha}{\sin \gamma} d\alpha$ (11)

and $\tan \gamma = \frac{\tan \psi}{\sin \alpha}$ (12)

(d) Finally, the total energy dissipated due to foam-core resistance against flange folding, plus the crushing of the core, of crush strength σ_f , associated with an n-flange element is given by:

$$E_4^{\text{tot}} = \underbrace{n(\pi/8)H^2\sigma_f C_n}_{E_4^{\text{Flex}}} + \underbrace{2\sigma_f H A_n}_{E_4^{\text{Crush}}} \quad (13)$$

where A_n is the effective cross sectional area occupied by given “star” element including the foam core contained within it. The geometry of the area could be triangular, square, pentagonal, or hexagonal depending on the cell shape. For the soccer-ball sphere, A_n is triangular and is defined by OAB, as shown in Figure 2.

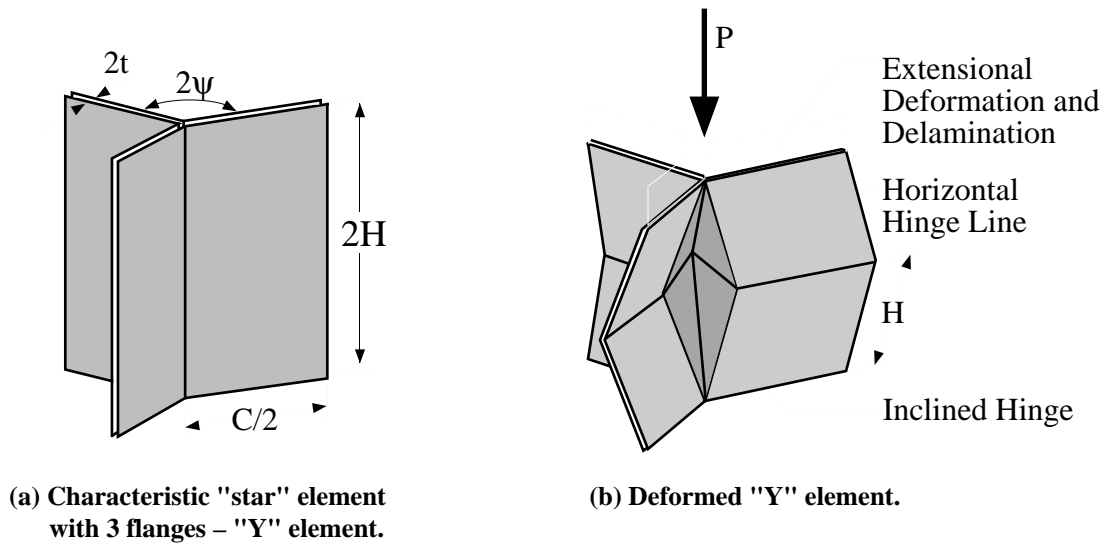


Fig. 27 - Schematic of a typical 3-flange element also referred to as “Y” element. For clarity the foam core contained within the flanges is not shown.

Assuming that the characteristic “star” element is folding with a wavelength of $2H$ under a mean load P_m , the energy balance for the element is given by:

$$2HP_m = E_1^{\text{tot}} + E_2^{\text{tot}} + E_3^{\text{tot}} + E_4^{\text{tot}} \quad (14)$$

which on substitution of equations (5, 8, 10 & 13) produces an expression for the mean crushing load for an n-flange “star” element:

$$P_m = 2n\sigma t b I_1^n + \frac{n\pi}{2H} C_n \sigma t^2 + \frac{n}{2b} \sigma t^2 H I_2^n + \frac{n\pi}{16} H \sigma_f C_n + \sigma_f A_n \quad (15)$$

With the parameters b and H being dependent on the condition of minimum energy (or load P_m) determined by:

$$\frac{\partial P_m}{\partial H} = \frac{\partial P_m}{\partial b} = 0 \quad (16)$$

Solution of equations (16) produces equations (17) and (18) in terms of the unknowns H and b:

$$H = \frac{4b^2}{t} \frac{I_1^n}{I_2^n} \quad (17)$$

$$\frac{\pi}{8} \sigma_f C_n b^4 + \sigma t^2 I_2^n b^3 - \frac{\pi}{16} C_n \sigma t^4 \left(\frac{I_2^n}{I_1^n} \right)^2 = 0 \quad (18)$$

Simultaneous solution of equations (17) and (18) and substitution of parameters b and H into equation (15) produces a value for the mean crushing load P_m for a single “star” element from which the mean crushing load for a given cellular structure can be obtained by summing up the contribution of each constituent “star” element.

Comparison with Experiment

Comparisons of crush load predictions with experimentally obtained values from quasi-static “Y”-element tests are presented in Figures 28-30 for cellular spheres 1-3, respectively. Crush load-prediction comparisons with “Y”-element tests are relatively straightforward since they are based on the contribution of an element of uniform cross-sectional area. Material property and geometry data used in the analytical predictions of “Y”-element and cellular sphere strengths are shown in Table 7. When the crush initiation peak and other global instability related features of the test responses are neglected, excellent agreement with the theoretical crush load values exists as shown in Figures 28-30.

Table 7 - Parameters used for crush load predictions of “Y”-elements and cellular spheres 2 and 4b.

Cellular Sphere	Web Length, C mm	Web Thickness, 2t Mm	Cell wall Strength, σ MPa	Foam Strength, σ_f MPa
1	73.15	3.40	204	1.10
2	73.15/65.13*	2.08	216	1.10
3	73.15	3.23	215	1.65
4a & 4b	63.66*	4.75	212	1.22 [†] /1.00

* Large cell-web length corresponding to cellular structures. The value is based on the outer radius of the cellular sphere.

[†] Value corresponding to sphere 4a.

There are at least two points worth noting from the “Y”-element series of testing. First there is the effect of foam core density, which can be deduced by comparing the response of cellular sphere 1 with sphere 3. Second there is the effect of cell wall thickness and strength as emphasized by the comparison of cellular sphere 1 with sphere 2. Experimental results show that the 30% increase in foam density resulted in nearly 50% increase in effective core strength and approximately 17% increase in “Y” element average sustained crush strength, which was also verified by the theoretical predictions. A greater effect on sustained crush strength was observed for samples of the same core material but of different cell wall thickness. The 39% decrease in cell wall thickness resulted in approximately 34% decrease in sustained crush strength, which was also predicted by the theory.

As opposed to a single “Y”-element, treatment of the cellular sphere crush loads is a much more challenging task for the following reasons:

- (a) The experimental crush load is not measured directly. It is the product of the estimated average acceleration of a multi-mass body, and the effective mass of a non-rigid body.
- (b) The cross section of the cellular sphere varies as $\pi h(D-h)$ where D is the sphere diameter and h is the crush distance.
- (c) Unless the impact is perfectly central not all “Y” elements are engaged at the same angle relative to the impact direction.
- (d) The flange length of each “Y” element is a function of the crush distance h .

Correlation of the initial sustained crush loads with theoretical predictions is presented in Figure 31 for cellular spheres 2 and 4b. Bearing in mind these limitations and the additional fact that the static crush value for the polyurethane core of cellular sphere 2 was used, the theory appears to correlate well with the experiments as indicated by the horizontal lines marking the theoretical impact accelerations. Impact accelerations were determined by dividing the crush load by the total mass.

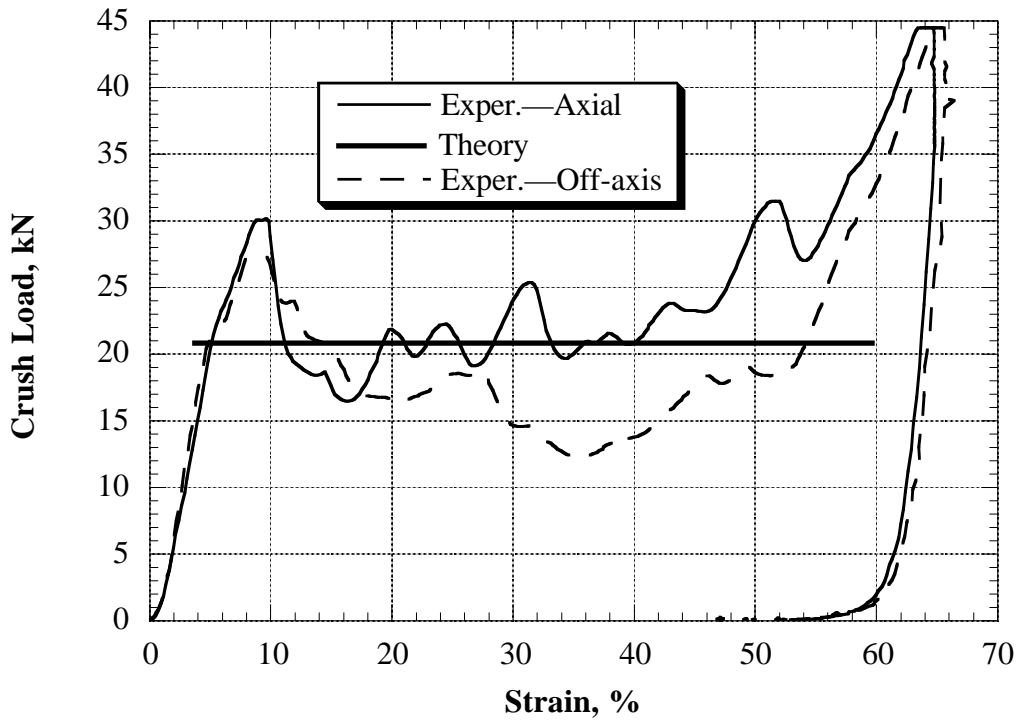


Fig. 28 - Comparison of predicted crush loads with typical crush responses of “Y” element samples from cellular sphere 1.

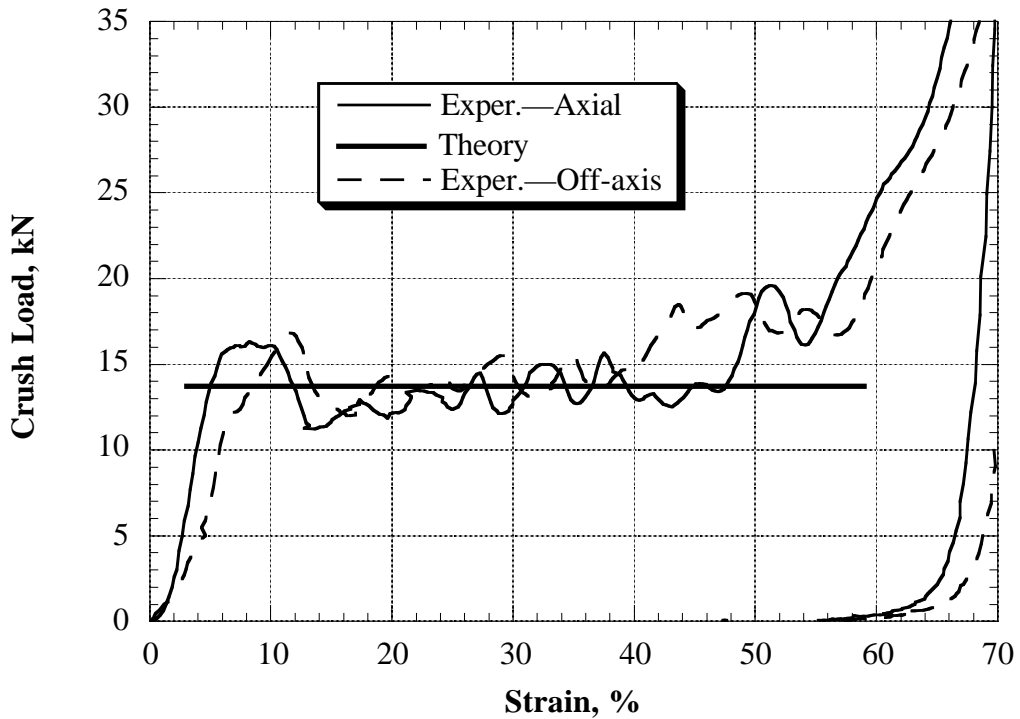


Fig. 29 - Comparison of predicted crush loads with typical crush responses of “Y” element samples from cellular sphere 2.

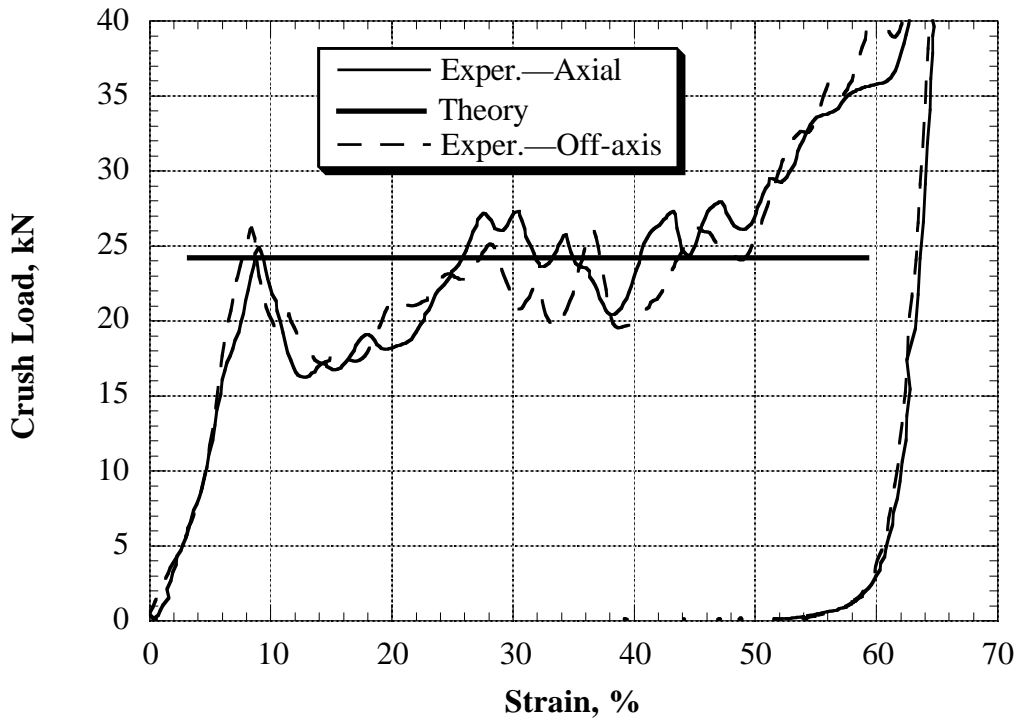


Fig. 30 - Comparison of predicted crush loads with typical crush responses of “Y” element samples from cellular sphere 3.

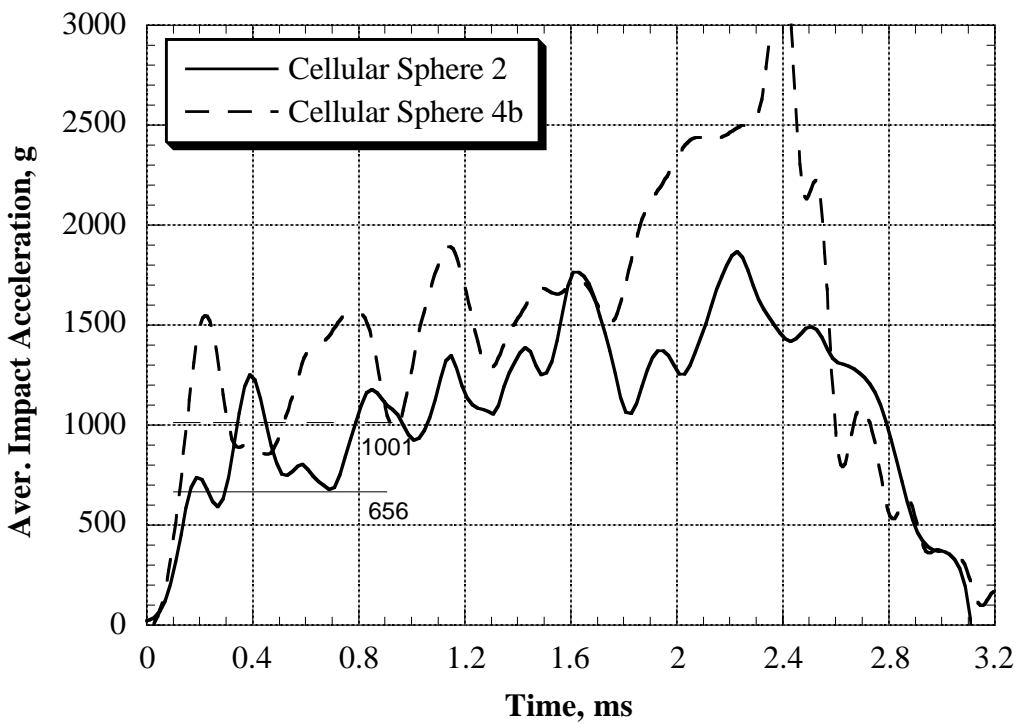


Fig. 31 - Comparison of theoretical predictions with the initial average impact accelerations of cellular spheres 2 and 4b.

Summary

It was shown that a cellular sphere concept is sufficient to meet the preliminary requirements for energy absorption of a passive Earth entry vehicle. The cellular sphere 4b, which met all preliminary mission requirements for mass and impact velocity, offered adequate protection with maximum loads limited to 14% lower than the allowable level of 3500 G for a hard surface impact.

Fabrication and materials

Test-to-test uniformity of the cellular sphere crush response indicated that the concept is relatively insensitive to fabrication irregularities such as cell wall thickness. So far as fabrication quality is concerned, perhaps the most critical component of the cellular sphere proved to be the inner spherical shell, which reacted the crush loads and helped isolate the OS from the stress concentration of the cell-webs and their junctions.

The resin infusion technique used for five cellular sphere samples proved to be well suited to the present design objectives and specimen configuration. However, depending on the final choice of materials and/or sphere architecture (total number of cells), a different method may be more appropriate. In particular, molding individual cell cups and inserting the foam core in a secondary process may be a more viable method for assembling a cellular sphere of a higher count of cells, such as for example the 60-triangle alternative.

For the general purpose of this conceptual study, the choice of materials proved to be acceptable. However, large improvements in crush performance are anticipated if fiber reinforcement orientation is optimized further. Fiber placement and/or custom polar fabrics could be used to take full advantage of the material's anisotropic nature. The added cost factor for such an implementation has not been considered in this study.

Results from spheres 4a and 4b have indicated that a separate penetration shield of loose kevlar layers as opposed to the hybrid co-cured alternative offers better post-crush integrity, containment, and possibly better penetration resistance. However, poor coupling between the brittle graphite outer shell and cell webs led to a poor energy-absorbing response. Consequently, it is recommended that a combination of the two shield methods be used, especially when penetration resistance becomes a necessary design requirement. The hybrid co-cured shell should be used to maintain adequate integrity and hence transverse support to the cell webs and the loose kevlar-29 cover should be added externally in a secondary process for improved penetration resistance. A mass penalty is anticipated with this approach depending on the required level of penetration protection.

Sphere geometry

For the present range of mission requirements the “soccer ball” approach appears to offer a well-balanced collection of features such as near-rectangular crush pulse, large crush stroke, good post-crush integrity, and manageable stress concentrations at the inner shell interface. Alternative sphere architectures have also been proposed and can be studied analytically using the generalized theory developed and validated in this study.

Theory

Theoretical crush load predictions based on the crush strength of individual cell wall junctions (or elements) appear to correlate well with the experimental data. The theory is general enough and can be used, within its limitations, for the design of cellular structures of various geometries, and or cell configurations.

References

- [1] Mitcheltree R., Braun R., Hughes S. and Simonsen L. “Earth-Entry Capsule for Mars Sample Return,” IAF-00-Q.3.04, 51st International Astronautics Federation Congress, Rio de Janeiro, Brazil, Oct. 2-6, 2000.
- [2] Kellas S., “An experimental investigation into the energy absorption performance of composite beam web for aircraft subfloor applications,” National Technical Specialists' Meeting on Rotorcraft Structures, “Design Challenges and Innovative Solutions,” Sponsored by the AHS, Oct. 1995.
- [3] Kellas S. and Knight N. F. Jr., “Design, Fabrication and Testing of Composite Energy-Absorbing Keel Beams for General Aviation Type Aircraft,” AIAA-2001-1529, 42nd AIAA/ASME/ASCE/AHS/ASC Structures, Structural Dynamics, and Materials Conference and Exhibit, Seattle, WA, April 16-19, 2001.
- [4] Kellas S. and Carden H. D. “Crash-energy absorbing composite structure and method of fabrication”, US Patent # 5,746,537, May 5, 1998.
- [5] Hayduk R. J. and Wierzbicki T. “Extensional collapse modes of structural members,” NASA Conference Pub. 2245, *Research in Structural and Solid Mechanics*, 1982.
- [6] Wierzbicki T., “Crushing Analysis of Metal Honeycombs,” *Int. J. Impact Engineering*, Vol.1, No.2, pp.157-174, 1983.
- [7] Wierzbicki T. and Abramowicz W., “On The Crushing Mechanics of Thin-Walled Structures,” *J. of Applied Mechanics*, Vol. 50, pp.727-734, 1983.
- [8] Abramowicz W. and Jones N., “Dynamic Progressive Buckling of Circular and Square Tubes,” *Int. J. Impact Engineering* Vol. 4, No. 4, pp. 243-270, 1986
- [9] Abramowicz W. and Wierzbicki T., “Axial Crushing of Multicorner Sheet Metal Columns,” *J. Applied Mechanics*, Vol. 56, pp.113-120, 1989.

- [10] Kellas S., "Experimental Characterization of Carbon Foams for Crash Energy Management", Crash Safety Challenges and Innovative Solutions, AHS, National Technical Specialists' Meeting on Rotorcraft Crashworthiness, Phoenix AZ, Sept. 14 - 16, 1988.
- [11] Lavoie J. A. and Kellas S., "Dynamic Crush Tests of Energy Absorbing Laminated Composite Plates," *Composites: Part A 27A*, pp. 467-475, May 1996.

